Hydrothermal synthesis of photoactive nitrogen- and boron- codoped TiO$_2$ nanoparticles for the treatment of bisphenol A in wastewater: Synthesis, photocatalytic activity, degradation byproducts and reaction pathways

Wael H.M. Abdelraheem[a,b,1], Meghshyam K. Patil[a,c], Mallikarjuna N. Nadagouda[d], Dionysios D. Dionysiou[a,*]

[a] Environmental Engineering and Science Program, Department of Chemical and Environmental Engineering (ChEE), University of Cincinnati, Cincinnati, Ohio 45221-0012, USA
[b] Chemistry Department, Faculty of Science, Sohag University, Sohag 82524, Egypt
[c] Department of Chemistry, Dr. Babasaheb Ambedkar Marathwada University, Sub-Campus Osmanabad, 413501, India
[d] Department of Mechanical and Materials Engineering, Wright State University, Dayton, Ohio 45324, USA

ARTICLE INFO

ABSTRACT

Hydrothermal technique was employed for the synthesis of N- and B-codoped TiO$_2$ at different atomic percentages and calcination temperatures (350 and 400 °C). Borane *tert*-butylamine complex was used as a novel precursor for the dopant atoms. The photocatalytic activities of catalysts were evaluated for destruction of bisphenol A (BPA) spiked in clean water and in secondary treated wastewater influent (SWI) collected from the Groundwater Replenishment System GWRS (Orange County, CA, USA), the world's largest water purification system for indirect potable reuse. Results of X-ray photoelectron spectroscopy (XPS) revealed the incorporation of N and B atoms onto TiO$_2$ lattice via substitution of O and/or Ti, and interstitial incorporation mechanisms. Carbon doping (graphite-like carbon; O-C = O) was also evidenced from XPS spectra. X-ray diffraction (XRD) and high-resolution transmission electron microscopy (HR-TEM) revealed pristine TiO$_2$ and all doped TiO$_2$ existed in anatase structure. The anatase phase of catalysts was further confirmed by simulation of selected area electron diffraction (SAED) of the catalysts and reported anatase TiO$_2$ using the simulation software CrysTBox (v 1.10). Among all prepared catalysts, 2.0NBT-350 (N + B = 2.0%, calcination = 350 °C) possessed the smallest particle size (12.9 nm), largest BET surface area (108.5 m^2/g) and highest visible-light absorption (i.e., λ > 400 nm). Simulated solar light/2.0NBT-350 system exhibited the maximum removal of BPA (0.1 μM) at the optimum catalyst dose of 0.8 g/L in clean water, over three consecutive degradation reuse cycles without any noticeable decrease in its photocatalytic activity. BPA was also successfully removed in SWI water, however with slower kinetics due to hydroxyl radical quenching effect of dissolved organic and inorganic species present in the SWI matrix. Degradation byproducts were identified by LC/Q-TOF-ESI-MS analysis. Six byproducts were found in the reaction mixture, with two compounds were newly identified in the current study. BPA oxidation routes comprised successive BPA hydroxylation, elimination of aromatic ring, ring opening, and cyclization of aliphatic compounds. This study is a promising demonstration for controlled design and synthesis of photocatalysts useful for environmental applications, especially for the treatment of BPA in wastewater effluents.

1. Introduction

Titanium dioxide (TiO$_2$) has been widely recognized as an environmentally friendly, easy to prepare, stable, and cheap catalyst with light activity, mainly in the UV region. These characteristics were the driving force for the extensive use of TiO$_2$ material in various fields including dye-sensitized solar cells, photocatalytic hydrogen production, and in environmental remediation purposes such as water treatment [1–8]. TiO$_2$-based AOPs showed capacity to destroy several environmentally recalcitrant pollutants such as humic acids, polysaccharides and conjugated aromatic compounds found in water [9]. However, the weak visible light absorbance has been one of the

Table 1
Catalysts IDs and corresponding synthesis conditions.

Catalyst ID[a]	Catalyst composition	wt. of Borane *tert*-butylamine complex (g)	Actual doping (atomic %) by XPS			Calcination temperature (°C)
			N	B	N + B	
TiO$_2$	Pristine TiO$_2$	0	0	0	0	350
0.9NT-350	N and TiO$_2$	0.1076	0.9	0	0.9	350
0.8NT-400	N and TiO$_2$	0.1076	0.8	0	0.8	400
2.0NBT-350	N, B, and TiO$_2$	0.2152	1.3	0.7	2.0	350
2.4NBT-350	N, B, and TiO$_2$	0.3228	1.3	1.1	2.4	350

[a] The catalyst ID was set to represent the total (N + B) doping % in the catalysts as calculated from xps analysis in Fig. 4 and Fig. S3.

critical limitations of TiO$_2$ against application in the field of water treatment. Consequently, tremendous efforts were devoted to improving photocatalytic properties of TiO$_2$ via extending its light absorption towards visible light region. Non-metal doping for TiO$_2$ proved to be one of the most competent methods used to reduce the wide bandgap characterizing pristine TiO$_2$ (i.e., 3.0–3.2 eV), and hence, promote the absorption of visible light which is a significant component in solar radiation. In this method, non-metal elements (e.g., B, C, F, N, P and S) with similar ionic radii to oxygen are introduced to TiO$_2$ particles via replacement of O in the lattice. This typically results in structural defects due to O-vacancies and renders TiO$_2$ visible light active [10–15]. Liu et al., for example, revealed the improved visible-light sensitivity of B-doped TiO$_2$ upon additional doping with N atom, which was rationalized by the formation O-Ti-B–N structure that facilitates the separation and transfer of charge carriers, and hence promoted the photocatalytic activity [16]. Recent advancements in TiO$_2$ doping have indicated codoping with two or more different atoms triggers even higher improvement in TiO$_2$ photocatalytic properties as compared to single atom doping [16,17]. According to Zhang et al., S, N and C codoped TiO$_2$ was shown to cause a faster visible-light driven degradation in microcystin-LR as compared to the non-doped TiO$_2$ [17].

Stimulated by the improved photosensitivity of non-metal doped TiO$_2$ in the visible light region and its potential applicability in the degradation of organic pollutants in water under solar light conditions, this study aimed at the synthesis of N- and B- co-doped TiO$_2$ simultaneously via simple hydrothermal technique, and to investigate the photocatalytic efficiency of synthesized nanomaterial for the degradation of bisphenol A (BPA) in water. BPA is a water-soluble, high production volume chemical. It has been used in the industry of several commercial products such as plastics, coatings of food cans, paints, sealants, flame-retardants, thermal papers and brake fluids [18,19]. According to the United States Environmental Protection Agency (U.S. EPA), there is a regular release of BPA to the environment at about 10^6 pounds/year [20]. As a result, BPA was found in several surface and groundwater samples in Europe and America at concentration levels 0.001–100 mg/m^3 [18]. It was also identified as an estrogenic compound with deleterious effects on humans, especially young generations, at as low concentration as 1 µg/m^3 [18]. With the above in mind, treatment of BPA in water has become a necessity to overcome its health-related issues.

In the current study, visible light sensitized N and B co-doped TiO$_2$ nanoparticles (NBT), containing pure anatase phase, were synthesized with a hydrothermal method, followed by calcination of the materials at 350 and 400 °C. Borane *tert*-butylamine complex was, for the first time, used as a substrate for N and B dopants. The synthesized photocatalysts were characterized by several techniques including X-ray diffraction (XRD), porosimetry analysis, high resolution transmission electron microscopy (HR-TEM), UV–vis diffuse reflectance spectroscopy (UV-DRS), X-ray photoelectron spectroscopy (XPS), and also by employing computer simulation using CrysTBox (v 1.10) software dedicated for identification of materials' crystallographic phases. The photocatalytic degradation of BPA was investigated under simulated solar

light. To optimize the degradation of BPA, the effects of dopant content (%), calcination temperature, catalyst loading, and initial concentration of BPA were investigated in Milli-Q water. The photocatalytic degradation of BPA was also studied in SWI water to compare the performance of the degradation system under real wastewater conditions. Finally, degradation byproducts from BPA degradation were identified by LC/Q-TOF-ESI-MS analysis technique, evolution kinetics were investigated, and degradation pathways were proposed.

2. Experimental

2.1. Chemicals and reagents

Titanium (IV) butoxide (> 97%, Ti(OCH$_2$CH$_2$CH$_2$CH$_3$)$_4$), borane *tert*-butylamine complex (97%, pellets), ethyl alcohol (≥ 99.5%, anhydrous) and acetic acid (≥ 99.85%, glacial) were used for TiO$_2$ synthesis. Bisphenol A (> 99%, 2,2-Bis(4-hydroxyphenyl)propane), STP (98%, Phthalic acid dipotassium salt), EDTA (99%, Ethylenediaminetetraacetic acid disodium salt dihydrate), 2 − OH-TP (97%, 2-Hydroxyterephthalic acid), *t*-BuOH (≥ 99.85%, tert-Butanol) were from Sigma Aldrich, USA.

2.2. Photocatalyst synthesis

Nitrogen- and boron- codoped TiO$_2$ nanoparticles were hydrothermally synthesized at three different borane *tert*-butylamine complex weights as a precursor for N and B (Table 1). Typically, a 7.0 mL of titanium (IV) butoxide was added dropwise to a 100 mL size Teflon hydrothermal vessel containing a mixture of 50 mL ethyl alcohol and 2.0 mL glacial acetic acid. Borane pellets were separately dissolved in 10.0 mL ethyl alcohol and then the solution was added to the previous mixture, followed by a dropwise addition of 2.0 mL Milli-Q water under vigorous stirring for 20 min at room temperature with the vessel's cap on. The mixture was then placed in a furnace at 180 °C for 20 h under a temperature ramp rate of 150 °C/h. The pale-yellow precipitate was then separated from the supernatant solution by decantation, dried at 80 °C for 6 h, then ground using a mortar. The last powder was transferred to a 50 mL clean porcelain crucible to be furtherly calcined at 350 °C for 10 h at 150 °C/h ramp rate. To reveal the change in photocatalytic properties of TiO$_2$ upon doping with N and B, pristine TiO$_2$ was also prepared for comparison purposes by the same method. In this experiment, a 10 mL pure ethyl alcohol was added to the hydrothermal vessel in lieu of the dopant solution. Table 1 depicts the abbreviations assigned for the synthesized catalysts (catalyst IDs) which will be used hereafter.

2.3. Catalysts characterization

Several spectroscopic and texture analysis techniques were utilized to characterize the prepared catalysts. The crystal phase and primary crystallite size of catalysts were identified by XRD analysis using a PANalytical Xpert Pro diffractometer with Cu Kα radiation

(λ = 1.5406 Å). The Brunauer, Emmett, and Teller (BET) surface area (m^2/g), pore volume (cm^3/g) and pore width (Å) of the photocatalysts were measured by dynamic N_2 adsorption measurement at $-196\,°C$ using a Tristar 3000 porosimeter analyzer (Micromeritics). The nanoparticle morphology and crystallinity were investigated using A JEOL (JEM-2010 F) high resolution-transmittance electron microscope (HR-TEM) with field transmission of 200 kV. To prepare the samples for HR-TEM, the catalysts were suspended in ethyl alcohol and sonicated for 30 min, then fixed on a Lacy Carbon-Copper grid (LC300-Cu, EMS) by drop-casting method. The optical properties and effective energy band gap (E_g) of the nanoparticles were studied by diffuse reflectance measurements using a UV–vis spectrophotometer (UV-2501 PC, Shimadzu) with an ISR 1200 integrating sphere attachment. Elemental composition and surface properties were investigated by XPS analysis performed by a Kratos Axis Ultra XPS system equipped with Al K X-ray radiation gun. The binding energies were corrected by C1 s level at 284.6 eV as a reference to reduce the relative surface charging effect.

2.4. Photocatalytic degradation of BPA and hydroxyl radical quantification

The photocatalytic activities of synthesized catalysts were assessed via degradation of BPA in Milli-Q water. The degradation experiments were conducted in a 100 mL borosilicate glass petri dish reactor containing 50 mL Milli-Q water, spiked with 1.0 μM BPA. The experiments were conducted without pH adjustments due to the insignificant change in pH during the reaction; initial and final pH values were 6.2 and 5.9, respectively. Four different catalyst loadings (i.e., 0.1, 0.2, 0.4 and 0.8 g/L) were tested. To check the potential adsorption of BPA on the catalyst, the reaction mixtures in all experiments were maintained covered with a quartz cover for 30 min in dark conditions under constant stirring prior to illumination. The reaction mixture was then subjected to a solar light from a solar light simulator manufactured by Newport (Irvine, USA) housing a Xenon lamp (500 W m^{-2}). The light was allowed to pass through a 7.5 cm diameter hole before it reached the surface of reaction solution (22 cm apart from the hole). Two light correction filters FSQ-GG420 and FSQ-KG5 from Newport (Irvine, USA) were used to obtain spectrum of light similar to that coming from the sun. The actual incremental spectrum of light emitted from the solar light simulator as a function of irradiance at the center of the petri dish reactor was measured by using A SpectriLight spectrophotometer model ILT950, Fig S1 (Supplementary information). Sampling was carried out at 0, 15, 30, 60 and 120 min of the illumination period.

To evaluate the performance of 2.0NBT-350 over reuse, the catalyst was collected after the degradation of 1 μM BPA, washed with Milli-Q water and dried at 60 °C using a drying lamp. The dried catalyst was then used (at the same dose; 0.8 g/L) for the degradation of a 1 μM BPA fresh solution (2nd reuse cycle). Again, the catalyst was collected, washed, dried and then employed for the third time to degrade a new 1 μM BPA solution (3rd reuse cycle).

Degradation of 1 μM BPA was also performed in SWI water from GWRS (Orange County, CA, USA) using simulated solar light/2.0NBT-350 at catalyst dose of 0.8 g/L, and an initial pH ~6.9 without further adjustment (final pH at the end of degradation experiment was ~6.2). Major characteristics of SWI water as provided by the GRWS facility in their 2017 Annual Report are summarized in Table S1 (Supplementary information) [21]. The received SWI sample was promptly filtered using Whatman glass microfiber filter paper (934-AH) to remove any suspended solids and then refrigerated at $-5\,°C$ for further use. Total organic carbon (TOC) content was measured by Shimadzu VCSH-ASI TOC Analyzer, while total alkalinity (mg $CaCO_3$/L) was determined according to AWWA standard method [22].

Quantification of residual BPA was performed by an Agilent HPLC (1100 Series) equipped with a photodiode array detector (PDA). Separation was carried out by a Supelco C18 column (150 mm × 2.1 mm, 5.0 μm) using a mobile phase consisted of 0.1% (v/v) formic acid in water and 100% acetonitrile at formic acid: acetonitrile ratio of

30:70 (v:v). The flow rate was set at 0.3 mL min^{-1}, with a sample injection volume of 50 μL, column temperature at 25 °C and detection wavelength of 221 nm.

In order to identify the main reactive species responsible for BPA oxidation during the photocatalytic degradation process, photocatalytic degradation experiments for 1 μM BPA by 2.0NBT-350 in 50 mL Milli-Q water were in presence of different scavengers including 1 mM EDTA, 20 mM t-BuOH and 2 mM STP. To further quantify hydroxyl radical generated during the process, a probe method was used [23]. In this method, 2 mM of STP was mixed with 0.8 g/L of 2.0NBT-350 in Milli-Q water (final volume 50 mL) in the glass reactor. Upon illuminating the last suspension with simulated solar light, $2-OH-TP$ was expected to gradually generate due to the selective attack of ˙OH to the carbon atom at *ortho*-position of STP [24]. The concentration of generated $2-OH$-TP, corresponding to ˙OH concentration, was monitored by measuring its corresponding fluorescent spectrum of the reaction solution at 624 nm using Shimadzu spectrofluorophotometer model RF-1501. The same experiment was repeated in the presence of SWI water instead of Milli-Q water to compare the concentration of hydroxyl radical generated in the two systems. Hydroxyl radical measurements were performed under simulated solar light irradiation at 0, 15, 30, 60 and 120 min, as well as after 30 min of dark reaction. Calibration experiment was conducted using $2-OH$-TP standard solution at 2, 4, 8 and 16 μM and results are shown in Fig. S2.

3. Results and discussion

3.1. Physicochemical properties of photocatalysts

Fig. 1 depicts XRD results of the synthesized photocatalysts. All diffraction patterns confirmed the existence of pristine and doped TiO_2 in monocrystalline, anatase phase (101), which was an expected result under the relatively low annealing temperature (i.e., 350 and 400 °C) used to prepare the catalyst [25,26]. The structure of catalysts did not change after doping as both pristine and doped TiO_2 possessed a similar lattice spacing (d = 3.5227 nm; based on Bragg's law) [26]. The low doping content (%) used in the current study and smaller radii of dopant atoms, compared to Ti and O, could explain the last observation. A similar result was also obtained by Zhang et al. (2014) for S, N and C co-doped TiO_2; a minor variation in lattice spacing (± 0.002 nm) was found between the pristine TiO_2 and the same material after doping [25].

The structure of synthesized materials was further investigated using HR-TEM analysis. Clear lattice fringes were obtained for pristine TiO_2 and 2.0NBT-350 catalysts as shown in Fig. 2c and g. Again, both
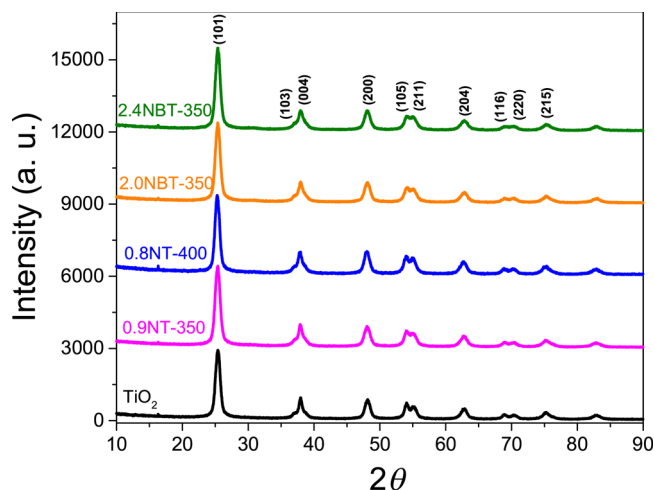

Fig. 1. XRD spectra of pristine and doped TiO_2 nanoparticles at different initial doping % and calcination temperatures.
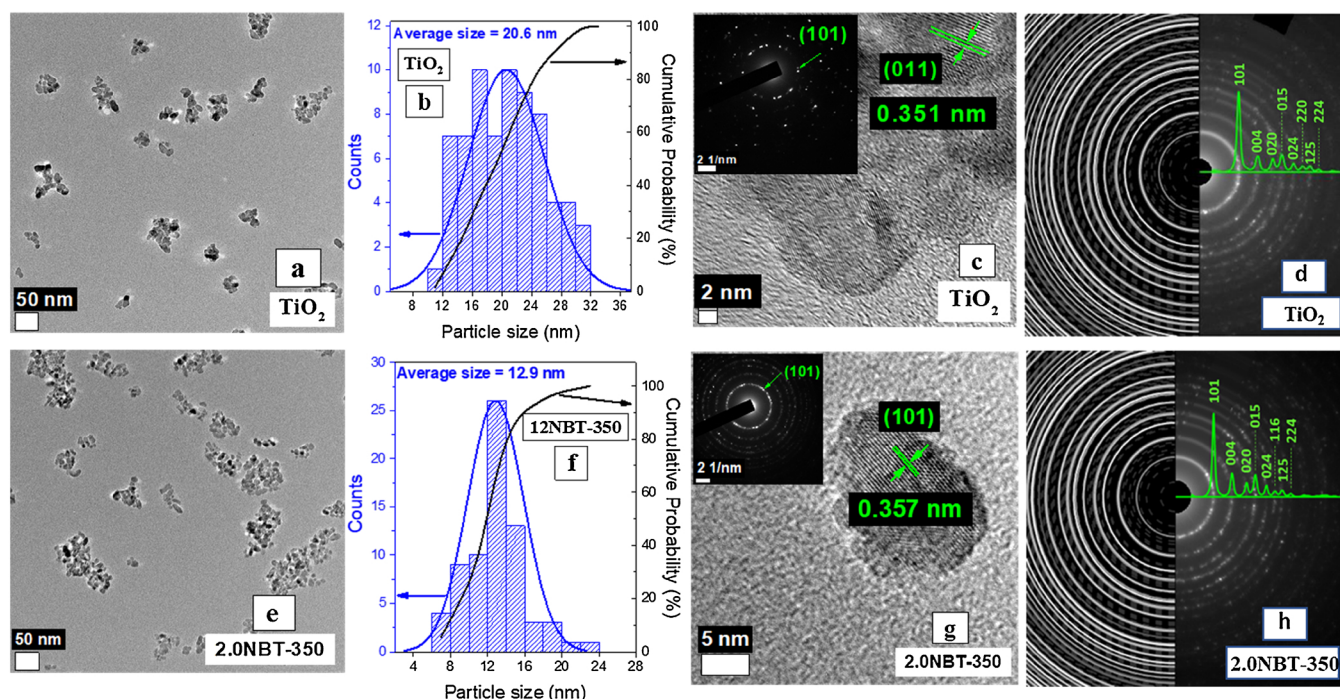
Fig. 2. TEM and HR-TEM micrographs and particles analysis for TiO_2 (a, b, c and d) and 2.0NBT-350 (e, f, g and h).
(a) & (e) TEM micrographs
(b) & (f) Particle size distribution and average size from 70 candidate particles
(c) & (g) HR-TEM image (*inset*: SAED pattern)
(d) & (h) Modelled SAED patterns (*done by* CrysTBox Server (v 1.1) software)

doped and pristine photocatalysts possessed a lattice spacing (*d*) of 0.34 nm, that was typical to the plane (101) in the anatase TiO_2 available in the online database (JCPDS 75–1537). Moreover, SAED patterns (the insets in Fig. 2c and g) confirmed the same anatase phase for TiO_2 and 2.0NBT-350. Klinger et al. have recently released a simulation software (CrysTBox v 1.10) that identifies the geometric phase of material by way of comparing experimental SAED data with a list of standard candidate materials, available in online crystallographic databases (e.g., Crystallography Open Database; COD) [27,28]. Besides, the software automatically generates the crystallographic diffraction pattern of the identified material and the corresponding Miller indices of each crystal plane. Using CrysTBox, experimental SAED patterns of pristine TiO_2 and 2.0NBT-350 were modeled to different TiO_2 materials (representing the most common phases of anatase, rutile, and brookite) until the best overlapping was achieved. The *left-sides* of Fig. 2d and h depict a complete overlapping of experimental and modeled SAED rings, while the *right-sides* exhibit the predicted diffraction patterns and corresponding Miller indices. Indeed, anatase phase was the predominant phase describing the SAED rings of pristine TiO_2 and 2.0NBT-350 materials. Moreover, the modeled diffraction patterns obtained by CrysTBox for both catalysts were highly similar to the experimental XRD results, although few diffraction peaks were not identified via modeling due to shoulder effect.

The average particle size of the catalysts was calculated from XRD analysis (using Scherrer's equation) and from TEM images (using the image processing software ImageJ, version 1.5i). According to XRD data, the average particle size was ~9 nm for all prepared catalysts, while, using TEM images (70 candidate particles were analyzed) was 20.6 and 12.9 nm for TiO_2 and 2.0NBT-350 catalysts, respectively, Fig. 2a, b, e, and f. The discrepancy in calculated particle size by the two methods was rationalized as Scherrer's equation only considers crystallite size, that is typically smaller than the particle size (i.e., a domain of several crystallites). Moreover, measurement of particle size from TEM images was generally performed by visualization technique

that took into account clumped small crystallites. According to Fig. 2 (b and f), TiO_2 catalyst maintained a wide particle size distribution (10–32 nm), with approximately 50% of the particles were below 20 nm in size. On the other hand, all doped material showed a narrower particle size distribution, especially 2.0NBT-350 catalyst that possessed a particle distribution range of 6–24 nm, with the majority of particles (90%) having size below 13 nm. Therefore, a higher surface area was expected for 2.0NBT-350 as compared to pristine TiO_2 and the remaining doped catalysts (*data not shown*).

Fig. 3a, b, c, and d depict the N_2 adsorption-desorption isotherms, average pore width and BET surface areas, pore volume, and UV-DRS spectra (**inset**: Tauc plot) of the prepared nanoparticles, respectively. The N_2 adsorption-desorption plots for all photocatalysts were consistent with Type IV isotherm, which is representative of mesoporous structures [29]. Compared to pristine TiO_2, all doped catalysts possessed increased surface areas, with the largest BET surface area of 108.5 m^2/g was recorded for 2.0NBT-350. Moreover, average pore diameter, pore width, and pore volume did not exhibit significant changes upon doping. Therefore, the change in surface areas of N- and B- codoped TiO_2, especially 2.0NBT-350, was attributed to their smaller particle size in comparison to pristine TiO_2.

With respect to pristine TiO_2, all doped materials showed enhanced visible light absorbance, with 2.0NBT-350 revealed the highest light absorption @ $\lambda > 400$ nm (Fig. 3d). Higher doping content (i.e., 2.4%) and elevated calcination temperature (i.e., 400 °C) tended to decrease the visible light absorption of TiO_2. Moreover, the effective band gaps (E_g; eV) of catalysts were calculated from Tauc plot by using Kubelka-Munk equation (Fig. 3d *inset*) [30]. The effective band gaps of photocatalysts and their corresponding light wavelength (λ) were in the following order $TiO_2 \sim 0.8NT$-400 (2.82 eV; $\lambda = 439$ nm) > 0.9NT-350 (2.80 eV; $\lambda = 443$ nm) > 2.4NBT-350 (2.78 eV; $\lambda = 446$ nm) > 2.0 NBT-350 (2.72 eV; $\lambda = 445$ nm). It is noteworthy noting that carbon atoms from the solvent was most likely participated in TiO_2 doping even in the absence of N and B dopants. This was apparent from the XPS
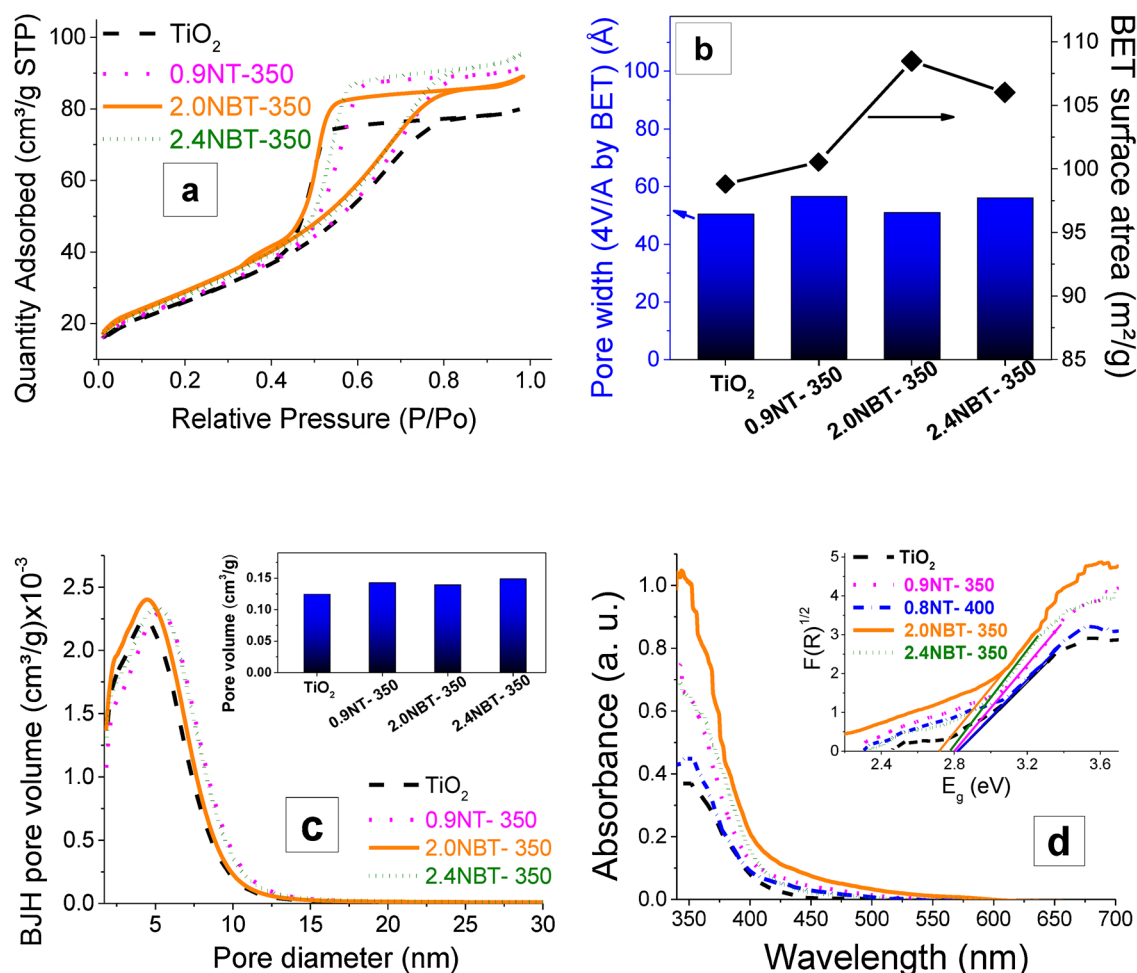
Fig. 3. Surface texture and photoelectronic analysis of catalysts.
(a) N_2 adsorption-desorption isotherm
(b) Average pore width (by BET) and BET surface area for different catalysts
(c) Pore volume vs. Pore diameter (*inset*: average BJH pore volume of different catalysts)
(d) UV-vis DRS of TiO_2 and NBT nanoparticles (*inset*: Tauc plot)

analysis for pristine TiO_2 and the doped TiO_2 as will be discussed hereafter. As a result, the band gap of TiO_2 in the current study (2.82 eV) was significantly lower than the reported value of anatase TiO_2 (~3.2 eV) [31]. Moreover, TiO_2 doping with N and B in the current study further improved the photoelectronic properties of the catalyst, with 2.0NBT-350 catalyst showed the narrowest energy band gap (2.72 eV) compared to the other synthesized photocatalysts.

XPS analysis was used to investigate the elemental composition of all catalysts (Fig. 4 and Fig. S3). The actual atomic percentages (%) of dopants N, B and N + B were calculated from the XPS analysis and results are shown in Table 1. Nitrogen existed in all doped catalysts, while boron was only found in 2.0NBT-350 and 2.4NBT-350 catalysts. The catalyst 0.8NT-400 exhibited slightly lower N content as compared to 0.9NT-350 which was explained by the low thermal stability of N at 400 °C. The survey scan performed on 2.0NBT-350 confirmed the existence of Ti, O, N, B, and C atoms in the structure (Fig. 4). The Ti 2p core levels recorded at binding energies 459.3 and 465.2 eV were characteristic peaks of Ti-O bonding in TiO_2, while, the small peak at 460.5 eV was attributed to O substitution with N atom in TiO_2 to form Ti-N bonding [32]. A similar result was previously observed for N-doped black Titania [33]. The O 1 s core level peak centered at binding energy 530.7 eV, and the shoulder peak at 532.2 eV were in good agreement with the reported values for bulk oxide (O^{2-}) and surface hydroxyl (OH) of TiO_2 [34]. The deconvolution results for C 1 s XPS peaks comprised three components at

binding energies 285.6 eV, 287.2 eV and 289.7 eV. The first peak could be assigned to graphite-like C–C bonding overlapping with C–H bonding of hydrocarbon from organic residue or possibly to carbon contamination from XPS instrument. The second XPS peak was ascribed to the oxidized form of carbon (i.e., C–O and C=O) that took place during the catalyst calcination [35]. The last peak intensity at 289.7 eV unveiled the existence of O–C=O bonding corresponding to graphite-like carbon species [25,35,36]. The absence of XPS peaks at the binding energies 282 and 288 eV implied that substitution of oxygen or Ti in 2.0NBT-350 with carbon was unlikely [37]. This result was previously reported for TiO_2 synthesized in an oxygen-rich atmosphere, which is typical to the current experimental conditions [17]. In case of pristine TiO_2, a small XPS peak at 282 eV was identified and ascribed to carbon doping via oxygen substitution in TiO_2 (Fig S3a). Two N 1 s XPS core levels were observed at 400 eV and 402.3 eV due to substitutional (Ti-N) and interstitial (Ti-O-N) incorporation of N atom onto the TiO_2 crystallite (Fig. 4) [33]. The deconvolution of the B 1 s XPS spectrum resulted in three peaks allocated at 189.3 eV, 190.4 eV and 192.6 eV binding energies. According to the literature, the low energy peak at 189.3 eV characterized O substitution with B atom in TiO_2 to yield the interstitial O-Ti-B, Ti-O-B or TiB_2 bonding. The second peak identified at 190.4 eV, corresponded to B–N bonding in Ti-N-B or Ti-B–N. The third peak at 192.6 eV was correlated to H_3BO_3 or B_2O_3 positioned on the surface of 2.0NBT-TiO_2 [38].

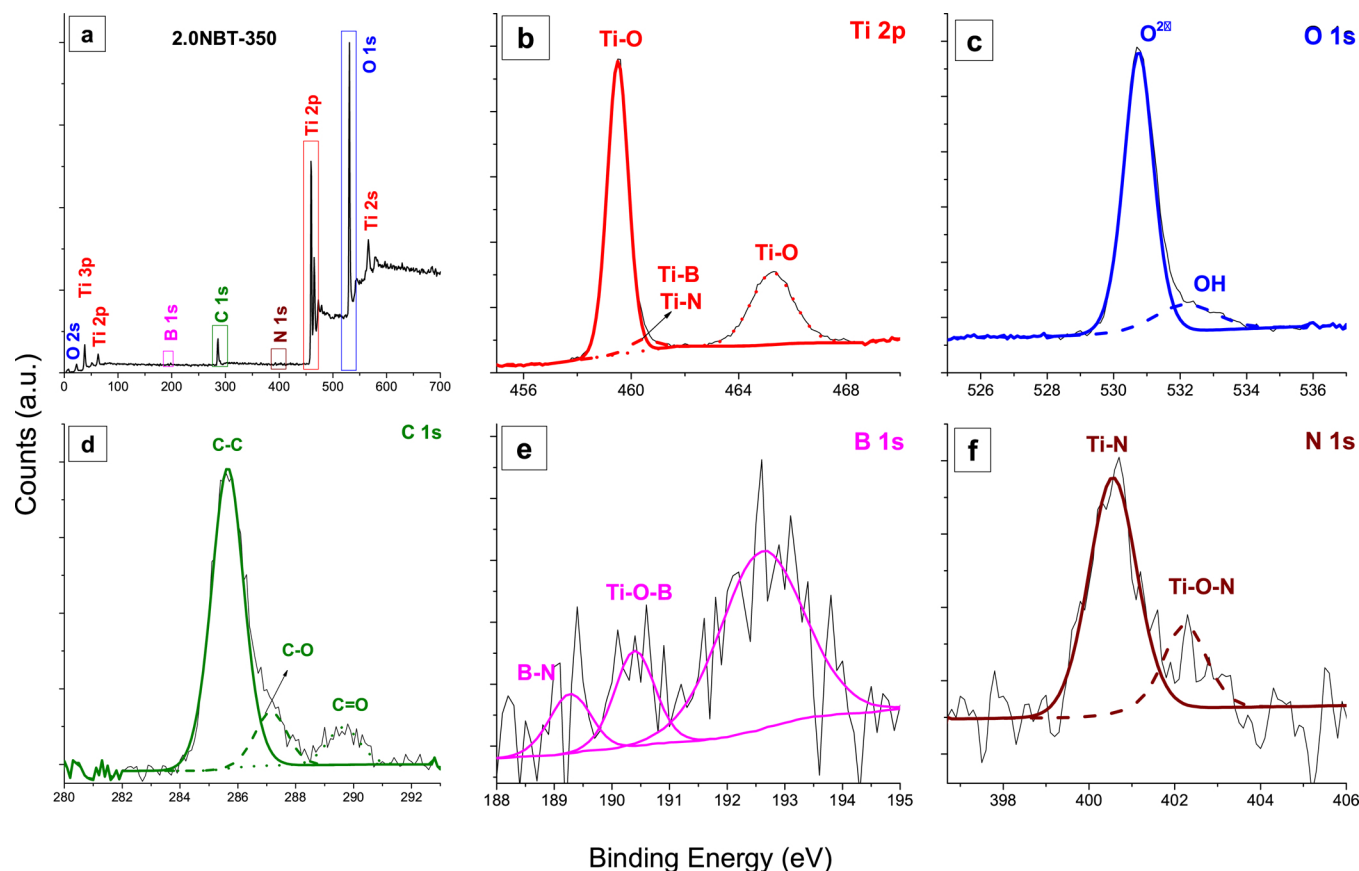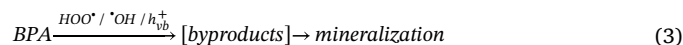**Fig. 4.** XPS surface analysis for 2.0NBT-350.

3.2. Photocatalytic oxidation of BPA

3.2.1. Role of TiO₂ and simulated solar light on BPA degradation

The photocatalytic activities of synthesized catalysts were investigated for BPA degradation in aqueous media under uncontrolled pH conditions (initial pH = 6.2). Fig. 5a depicts the adsorption/photocatalytic degradation of BPA by different oxidation systems. BPA did not suffer noticeable adsorption on TiO₂ catalysts under dark experimental conditions. The electrostatic interaction between TiO₂ and organic compounds was previously shown to be dependent on both point-of-zero charge (PZC) of TiO₂ and pH of the medium [39]. That is, TiO₂ surface (PZC = 6.25) become positively charged in acidic medium (pH < PZC) and negatively charged in basic medium (pH > PZC). According to the dissociation constant of BPA (pK_a = 9.6), it can only adsorb onto negatively charged TiO₂ surface in strongly basic medium (pH > pK_a) [40]. Therefore, the absence of electrostatic attraction/adsorption between BPA and all TiO₂ catalysts in the current study was probably due to the near neutral condition of the reaction medium. Under simulated solar light only condition, again there was no noticeable degradation in BPA which was explained by the poor light absorbance (very low extinction coefficient) of BPA at λ > 300 nm, especially in acidic and neutral media [41,42]. BPA degradation was only initiated by simulated solar light/TiO₂ system, which indicated the essential role of TiO₂ and simulated solar radiation in BPA degradation (Fig. 5a). Moreover, photocatalytic removals of BPA by all N- and B-codoped catalysts were notably higher than by pristine TiO₂, which was likely attributed to the improved photocatalytic properties of doped TiO₂.

TiO₂ was previously shown to be a photoactive material that upon illumination with a suitable light source (with energy ≥ band gap ~3.2 eV), electron (e^-)-hole (h^+) pairs are generated at the interfacial surface (Eq. (1)) [43]. In this process, the valence-band (VB) electrons

(e_{vb}^-) are excited by the incident light and migrate to a higher energy level (i.e., conduction-band) (e_{cb}^-), leaving behind positively-charged holes (h_{vb}^+). The surface e_{cb}^- was reported to interact with dissolved oxygen in aqueous media and generate reactive oxygen species (ROS, e.g, $O_2^{\cdot-}$, HOO˙ and ˙OH) (Eqs. (2)). These ROS are capable of destroying organic compounds via successive bonds breakdowns and ultimately lead to their mineralization (Eq. (3)) [44,45]. It is also possible for organic compounds to be directly oxidized by h_{vb}^+ at the catalyst surface, and eventually be eliminated from the solution [46]. Accordingly, photocatalytic degradation of BPA by the different AOPs used in the current study could be explained.

$$TiO_2 + hv \rightarrow e_{cb}^- + h_{vb}^+ \tag{1}$$

$$e_{cb}^- + O_2 \rightarrow O_2^{\cdot-} \xrightarrow{H^+} HOO^{\cdot} \tag{2}$$

$$BPA \xrightarrow{HOO^{\cdot}/{}^{\cdot}OH/h_{vb}^+} [byproducts] \rightarrow mineralization \tag{3}$$

3.2.2. Effect of calcination temperature and dopant content (%) on BPA photocatalytic degradation

According to Fig. 5a, the degradation of BPA by 0.1 g/L 0.9NT-350 was slightly higher than that obtained by 0.8NT-400, especially at longer reaction time. This illustrated the important role of optimization of calcination temperature for doped TiO₂ catalysts. The higher calcination temperature (i.e., 400 °C) led to a decrease in 0.8NT-400 visible light absorption due to some loss of its dopant atom (i.e., N), and as a result its photocatalytic activity decreased. This was also consistent with the increased band gap of 0.8NT-400 (2.82 eV) as compared to 0.9NT-350 (2.80 eV). The impact of calcination temperature (i.e., 300–600 °C) on the photocatalytic properties of boron doped-TiO₂ (B-TiO₂) was previously discussed [47]. At elevated calcination temperature (> 400 °C), B-TiO₂ tended to lose its dopant atom due to
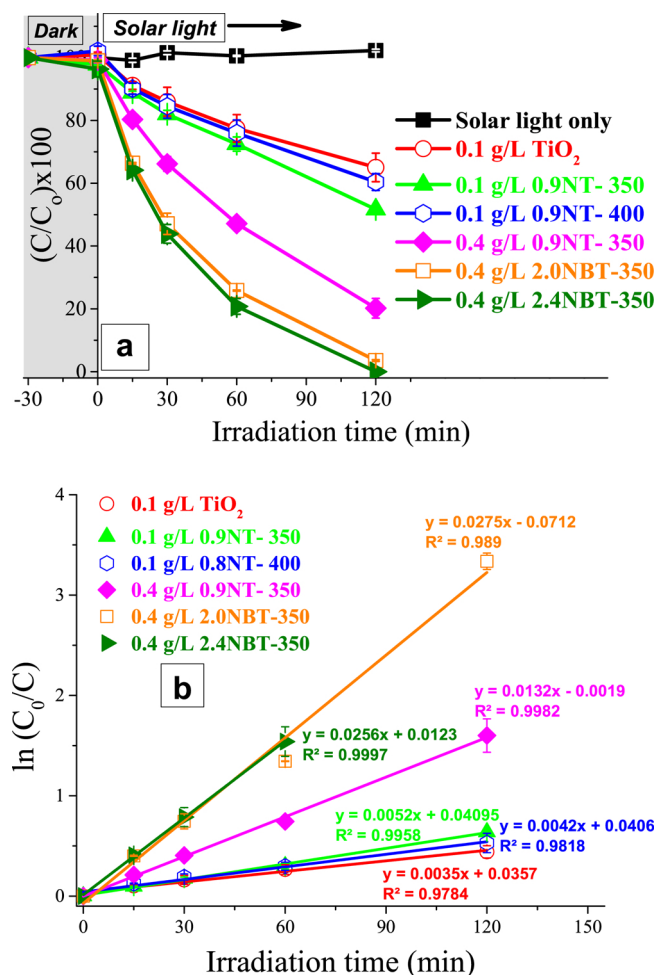
Fig. 5. a) Degradation of 1 μM BPA by simulated solar light, simulated solar light/TiO$_2$ and simulated solar light/doped TiO$_2$ at different doping percentages, calcination temperatures and catalyst dose. (b) *Pseudo-first-order* curve fittings for the degradation systems in Fig. 5a.

dissociation of Ti−O−B bond. Consequently, the B-induced visible light absorption of B-TiO$_2$ decreased and resulted in an inhibition of the photocatalytic activity of the catalyst [26,47]. With the above observation in mind, the optimum calcination temperature for N- and B-codoped TiO$_2$ synthesis was 350 °C.

To investigate the effect of TiO$_2$ doping content (%) on BPA degradation, photocatalytic degradation experiments were performed in the presence of 0.9NT-350, 2.0NBT-350 and 2.4NBT-350 at fixed 0.4 g/L catalysts dose (Fig. 5a). At 60 min, about 53% of 1.0 μM initial BPA was removed by 0.9NT-350 catalyst. BPA removal increased to 74% and 79% upon using 2.0NBT-350 and 2.4NBT-350, respectively. After 120 min, BPA was entirely removed by 2.0NBT-350 and 2.4NBT-350, while only 80% of BPA was removed in the presence of 0.9NT-350. The photocatalytic activities of the three catalysts were further compared with respect to the degradation kinetics. Thus, the degradation data in Fig. 5a were fitted to *pseudo-first-order* kinetics according to Eq. 4 (Fig. 5b). C_O and C are BPA initial and equilibrium (at reaction time t) concentrations (mM), k_{obs} is the *pseudo-first-order* rate constant (min^{-1}) and t is the irradiation/reaction time (min).

$$ln\frac{C_0}{C} = k_{obs} \bullet t \tag{4}$$

Values of k_{obs} obtained from data fitting the degradation data Table 2. The kinetics of BPA degradation by 2.0NBT-350 ($k_{obs} = 2.75 \times 10^{-2}$ min^{-1}) was twice as fast as by 0.9NT-350 ($k_{obs} = 1.32 \times 10^{-2}$ min^{-1}) and quite higher than by 2.4NBT-350 ($k_{obs} = 2.56 \times 10^{-2}$ min^{-1}). Thus, 2.0NBT-350 demonstrated the highest photocatalytic activity compared to the remaining catalysts (sec. 3.1). Further degradation experiments were, accordingly, conducted by using 2.0NBT-350 as a photocatalyst.

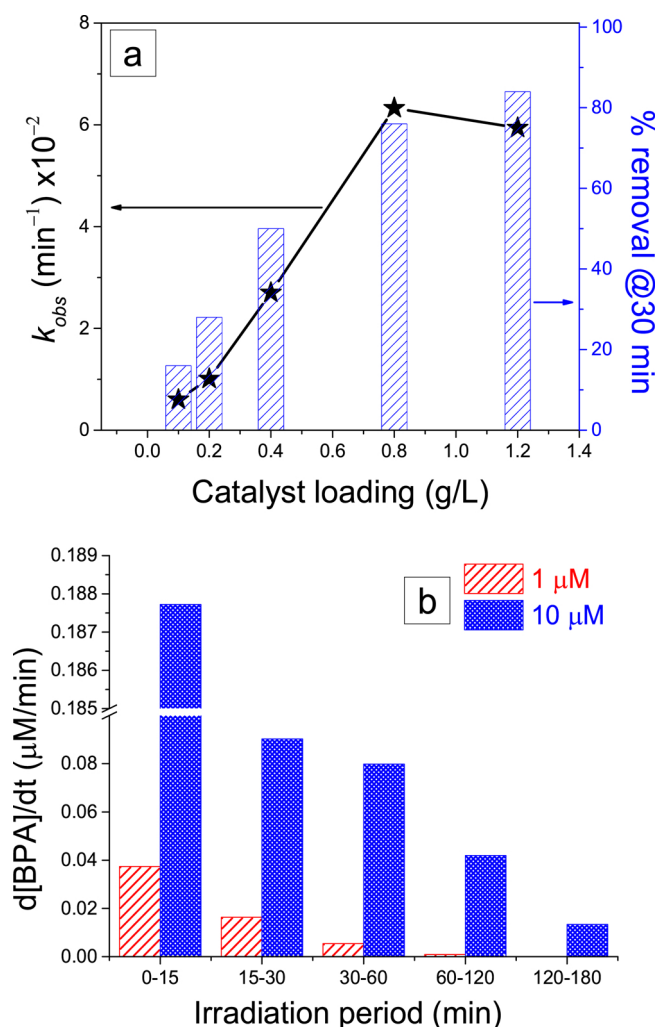*3.2.3. Effect of catalyst loading and initial BPA concentration*

The degradation of BPA was markedly enhanced with the increase of initial catalyst loading and almost halted at higher catalyst loading Fig. S4a. For quantitative evaluation of the impact of catalyst loading on BPA degradation, % removal of BPA (at 30 min) and k_{obs} were plotted against the different catalyst loadings, Fig. 6a and S4b. The respective % removal and k_{obs} of BPA ramped from 16% and 0.60×10^{-2} min^{-1} in case of 0.1 g/L catalyst dose to 50% and 2.70×10^{-2} min^{-1} at 0.4 g/L catalyst. Upon increasing the catalyst dose to 0.8 g/L, the % removal and k_{obs} values increased to 76% and 6.33×10^{-2} min^{-1}, respectively. The further increase in catalyst dose to 1.2 g/L resulted in a slight improvement in BPA degradation to 84%, and the reaction proceeded with slower kinetics (i.e., $k_{obs} = 5.0 \times 10^{-2}$ min^{-1}). As the catalyst dose increased from 0.1 to 0.8 g/L, the available surface and active sites on the catalyst increased, and as a result, the rate of photoinduced formation of free radical species at the surface 2.0NBT-350 was consequently amplified and resulted in more oxidation to BPA. On the contrary, increasing the photocatalyst dose above 0.8 g/L probably caused a light-shielding effect that lessened the number of photocatalytic generated radicals

Table 2
Values of k_{obs} corresponding to BPA photocatalytic degradation at different experimental conditions, in presence/absence of scavenging agents and in SWI water.

Water matrix	[BPA]$_0$ (μM)	Photocatalyst	Quenching agent	Catalyst dose (g/L)	k_{obs} x10^{-2} (min^{-1})	R^2
Milli-Q water	1.0	TiO$_2$	–	0.1	0.35	0.978
		0.9NT-350	–		0.52	0.995
		0.8NT-400	–		0.42	0.982
		0.9NT-350	–	0.4	1.32	0.998
		2.0NBT-350	–		2.75	0.989
		2.4NBT-350	–		2.56	0.999
		2.0NBT-350	–	0.1	0.60	0.995
			–	0.2	1.01	0.999
			–	0.4	2.70	0.990
			–	0.8	6.33	0.983
			–	1.2	5.94	1.000
			t-BuOH (20 mM)	0.8	3.91	0.996
			STP (2 mM)		1.26	0.998
			EDTA (1 mM)		0.62	0.985
SWI water			–		3.03	0.989

Fig. 6. a) Effect of catalyst loading (g/L) on the degradation of 1 μM BPA. k_{obs} (left y-axis), and % removal of BPSA (right y-axis) due to 30 min simulated solar irradiation at different catalyst doses. (b) Rates of BPA transformation by 0.8 g/L 2.0NBT-350 under simulated solar light irradiation, at 1 and 10 μM initial BPA concentrations.

responsible for BPA degradation [48]. A similar result was previously reported for the photocatalytic decompositions of aniline and carbendazim pollutants by TiO₂ AOP. The catalyst overdoses induced a light-screening effect that diminished the overall degradation rate and pollutants removal [49,50]. Based on the above findings, 0.8 g/L was considered the optimum 2.0NBT-350 dose that resulted in the maximum BPA removal, at the current experimental conditions.

Since the concentration level of contaminants in natural water varies from a water system to another, it was reasonable to evaluate the photocatalytic efficiency of 2.0NBT-350 at low and high initial BPA concentrations. Fig. S5 reveals the degradation profile of 1 and 10 μM BPA by 0.8 g/L 2.0NBT-350 in water. BPA was effectively removed at both initial concentration levels, however, longer reaction times were required for the 10 μM BPA system to achieve the same removal ratios obtained at 1 μM BPA. Nevertheless, the increased initial pollutant concentration could promote the degradation rate of BPA (d[BPA]/dt, μM/min). According to Fig. 6b, the degradation rates at 10 μM BPA were much higher than those at 1 μM BPA, at all irradiation periods indicated. Due to the increased number of collisions between pollutant molecules and radical species at high BPA concentration, a larger number of pollutant molecules was oxidized and led to an overall improved reaction rate [51].

3.2.4. Contribution of h^+ and various ROS on BPA degradation, studies of BPA degradation in field wastewater, and catalyst recyclability

The major reactive species responsible for BPA oxidation were identified using scavenger method [52]. In these experiments, the conventional ·OH scavenger t-BuOH ($k_{·OH,t\text{-BuOH}} = 3.8\text{–}7.6 \times 10^8$ M⁻¹ s⁻¹) [53] was used and compared with STP due to its high affinity and selectivity towards reaction with ·OH ($k_{·OH,STP} = 3.3 \times 10^9$ M⁻¹ s⁻¹) [53,54]. The majority of previous studies reported EDTA as an excellent scavenger for h^+, however, they did not take into account the significant affinity of EDTA towards ·OH ($k_{·OH,EDTA} = 2.0\text{–}9.0 \times 10^9$ M⁻¹ s⁻¹) [55]. Thus, EDTA was used in the current study as a scavenger for both h^+ and ·OH. Results in Fig. 7a and Table 2 revealed the addition of t-BuOH resulted in ~40% inhibition in BPA degradation ($k_{obs} = 3.91 \times 10^{-2}$ min⁻¹), while the addition of STP caused 80% inhibition ($k_{obs} = 1.26 \times 10^{-2}$ min⁻¹). This result was consistent with the high affinity of ·OH towards STP as compared to t-BuOH, i.e., $k_{·OH,STP} > k_{·OH,t\text{-BuOH}}$. When EDTA was used, about 90% suppression in the photocatalytic reaction rate constant ($k_{obs} = 0.62 \times 10^{-2}$ min⁻¹) was observed. These observations revealed ·OH was the major oxidant in the system and was responsible for 80% BPA degradation, whereas h^+ and other reactive species (e.g., HOO· and O₂·⁻) were only responsible for 20% degradation in BPA.

For practical evaluation of the performance of the current photocatalytic system under treated wastewater environmental conditions, photocatalytic degradation of 1 μM BPA by simulated solar light/2.0NBT-350 was carried out in SWI water spiked with BPA. A comparison between BPA removal percentages ($\frac{[BPA]_0 - [BPA]}{[BPA]_0} x 100$) in Milli-Q water and in SWI water at different time intervals as well reactions rate constants (k_{obs}, min⁻¹) was established and results are shown in Fig. 7b, S6 and Table 2. BPA removal in Milli-Q water ($k_{obs} = 6.33 \times 10^{-2}$ min⁻¹) was almost two times faster than in SWI sample ($k_{obs} = 3.03 \times 10^{-2}$ min⁻¹). About 60% and 83% of initial BPA were removed in 15 and 30 min degradation period in Milli-Q water compared to only 30% and 54% in SWI water, respectively. Complete removal of BPA was reached in 60 min in Milli-Q water, though, the same illumination period was only sufficient for 84% removal in SWI water. BPA was fully degraded in SWI water at 120 min of photocatalytic degradation. The inhibition of BPA photocatalytic degradation in SWI water could be explained based on the chemistry (i.e., TOC and alkalinity) of SWI and the possible impact on the available ·OH responsible for BPA major degradation. In the current study, SWI water contained high TOC (9.834 mg/L) and total alkalinity content (163 mg as CaCO₃/L), as compared to Milli-Q water containing 1 μM BPA (i.e., TOC = 0.18 mg/L). The lower degradation rate of microcystin-LR (MC-LR) by UV₂₅₄ₙₘ/H₂O₂ AOP in natural water was previously explained by hydroxyl radical scavenging effect of organic and inorganic constituents of natural water [56]. Consequently, the observed inhibition in BPA degradation in SWI water was due to the scavenging effect of the photocatalytically generated hydroxyl radical species by the organic and inorganic contents of SWI water. To further confirm this result, the steady state concentrations of hydroxyl radical generated at certain irradiation periods were measured in Milli-Q and SWI water samples (Fig. 7b; solid curves and right y-axis). The ·OH concentrations in simulated solar light/2.0NBT-350/Milli-Q water system at 15, 30 and 60 min were 25, 39, and 76 μM, respectively. Almost half these concentrations (i.e., 13, 23 and 42 μM) were found in simulated solar light/2.0NBT-350/SWI water system. This result was consistent with the drop in k_{obs} of BPA photocatalytic degradation rate constant 6.33×10^{-2} min⁻¹ (in Milli-Q water) to 3.03×10^{-2} min⁻¹ (in SWI water). Indeed, the notable consumption of hydroxyl radical ·OH by the organic/inorganic content of SWI water was the major reason for the lower removal percentage/kinetics of BPA in the studied photocatalytic system.

Recyclability is one of the most important measures for catalyst efficiency over several reuses. Therefore, the 2.0NBT-350 was tested for
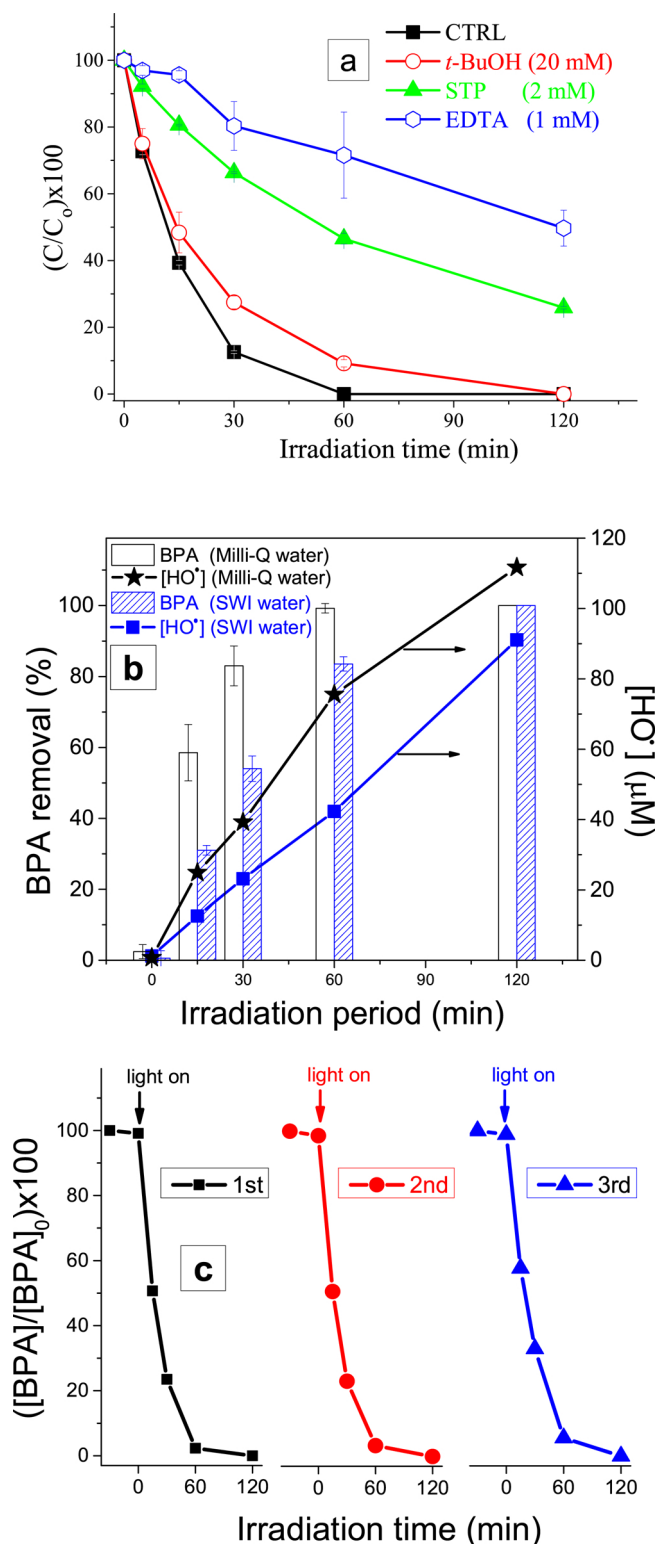
Fig. 7. a) Effect of different scavengers on BPA degradation. (b) Degradation of BPA in Milli-Q and SWI waters. (c) Catalyst recyclability; photocatalytic degradation of three consecutive utilization of 2.0NBT-350. Experimental conditions: catalyst dose = 0.8 g/L, $[EDTA]_0 = 1.0$ mM, $[STP]_0 = 2.0$ mM, $[t\text{-}BuOH]_0 = 20.0$ mM, and $[BPA]_0 = 1$ μM.

up to three photocatalytic degradation cycles as shown in Fig. 7c. Certainly, the catalyst showed an outstanding reuse performance; the same BPA removal efficiency was obtained for up to three reuse cycles. This identical photocatalytic activity over several recycles confirmed

the stability of 2.0NBT-350 in aqueous media, under simulated solar irradiation conditions.

3.3. Transformation byproducts and reaction pathway

3.3.1. Transformation mechanism and byproducts

The photocatalytic degradation of BPA by TiO_2 occurred at the catalyst-solution boundary via two major oxidation routes; i) oxidation by free radical species (i.e., majorly ·OH), and ii) oxidation/dehydration by h_{vb}^+ at the catalyst surface [57]. Earlier studies revealed ·OH to be the dominant oxidizing species in the solution at weak acidic to neutral pH, while h_{vb}^+ dominates only in strong acidic medium [58]. These findings were consistent with our results of using scavengers and with the pH condition (6.2–5.9) of the current degradation system. Therefore, the chemical structures of identified byproducts hereafter were suggested based on ·OH attack to BPA molecules.

Transformation byproducts were studied at high initial BPA concentration (10 μM) in presence of 0.8 g/L 2.0NBT-350. To identify the byproducts, the ion chromatograms extracted from LC/Q-TOF-ESI-MS experiment were analyzed based on peak area, retention time (*t*, min), mass-to-charge value (*m/z*) and the suggested chemical formula by the analytical software [59]. Using the aforementioned experimental set-up and strategies for data acquisition and analysis, six byproducts were identified, including mono-hydroxylated BPA (I-a or I-b, $C_{15}H_{16}O_3$, *m/z* 243), diketo compound 4-[2-(4-hydroxyphenyl)propan-2-yl]cyclohexa-3,5-diene-1,2-dione (II, $C_{15}H_{14}O_3$, *m/z* 241), 4-vinylphenol (III-a, $C_9H_{10}O$, *m/z* 133) or the keto derivative 4-(propan-2-ylidene)cyclohexa-2,5-dien-1-one (III-b, $C_9H_{10}O$, *m/z* 133), 4-hydroxyacetophenone (IV, $C_8H_8O_2$, *m/z* 135), and 5-oxohexenoic acid (V, $C_6H_8O_3$, *m/z* 127*i*) and its cyclic form 6-hydroxy-6-methyl-5,6-dihydro-2H-pyran-2-one (VI, $C_6H_8O_3$, *m/z* 127*ii*).

The evolution profiles of BPA and its byproducts, as represented by their corresponding HPLC peak areas, are demonstrated in Fig. 8. Almost 45% of initial BPA was successfully removed by simulated solar light/2.0NBT-350 in the first 15 min of the reaction. Compound I recorded its maximum release at 15 min, while the byproducts II, III and IV were quickly evolved and reached 26, 55 and 54% of their respective maximum abundance in the solution. Yet, compounds V and VI were not detected in the solution during that time frame. The byproduct II continued forming after 15 min with the same degradation kinetics and peaked at 30 min, then a sudden decay in its peak was observed up to 60 min followed by a slower decay until it was completely removed at 120 min. The evolution kinetics of compounds III and IV were much
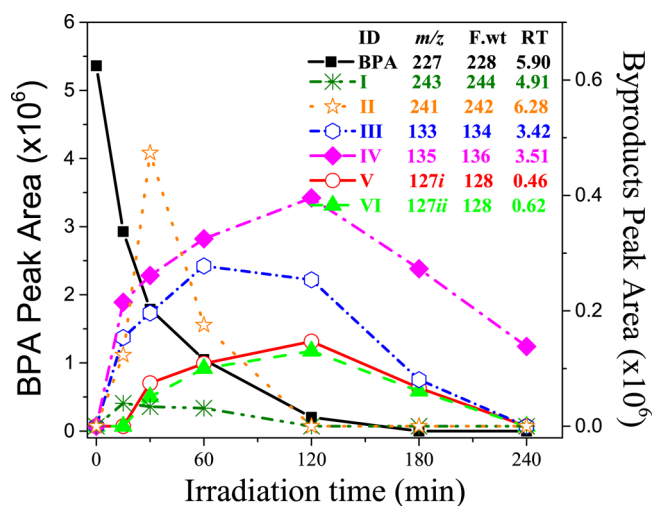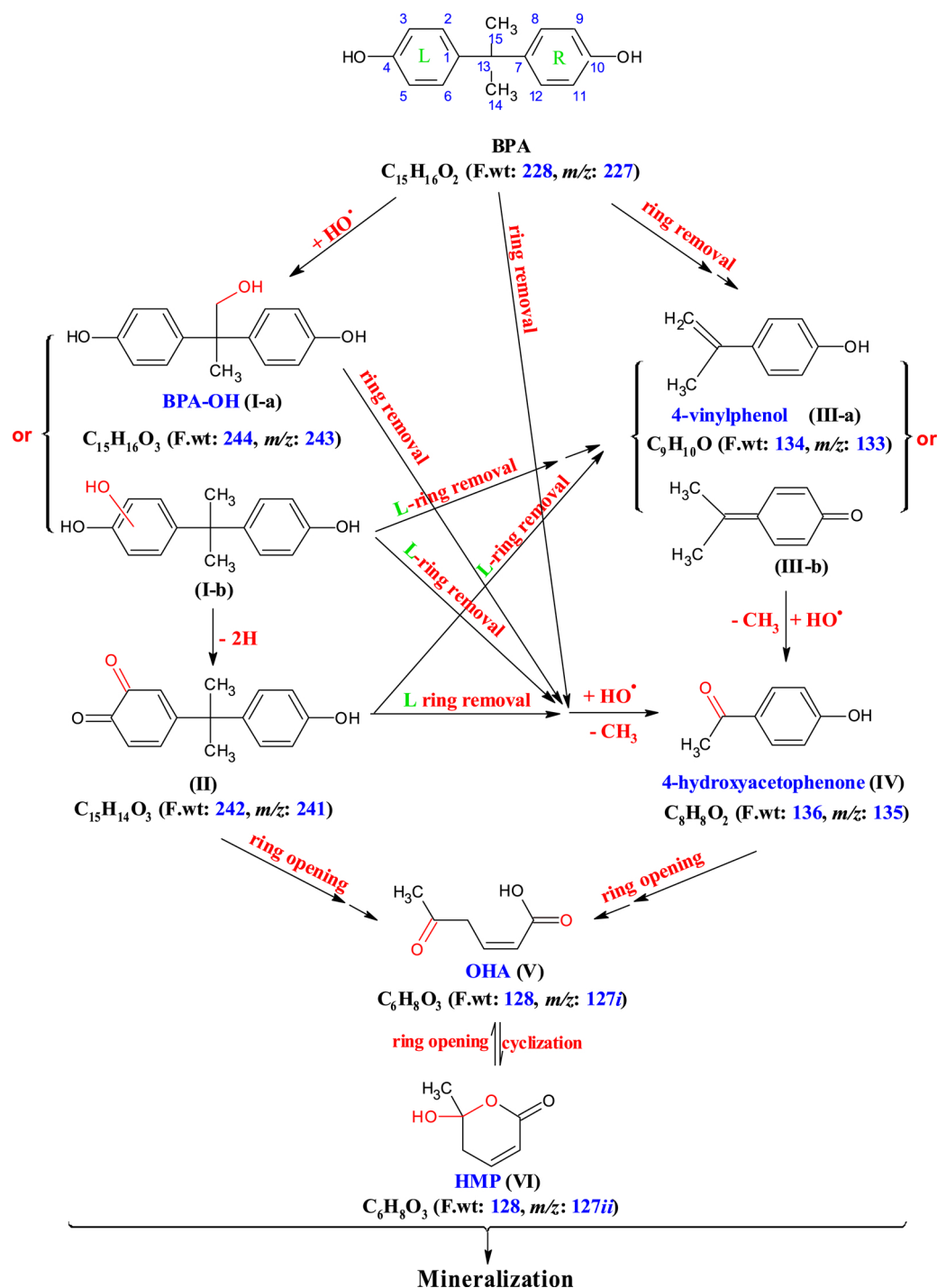

Fig. 8. Evolution profiles of major byproducts from BPA photocatalytic degradation by using LC/Q-TOF-ESI-MS technique. Experimental conditions: catalyst dose = 0.8 g/L and $[BPA]_0 = 1$ μM $[BPA]_0 = 10$ μM.

Scheme 1. Potential degradation pathways of PBSA.

slower after 15 min, with their maximum release recorded at 60 and 120 min, respectively. The last byproducts afterward showed different susceptibilities towards hydroxyl radical attack, that compound III was completely removed at 240 min when compound IV persisted in the solution at nearly 35% of its maximum abundance. As per compound I, it began decomposing slowly after 15 min, and entirely disappeared at 120 min. Compounds V and VI exhibited comparable evolution profiles after 15 min, i.e., a rapid evolution up to 30 min, followed by a relatively slower formation up to 120 when they peaked, and finally a rapid decay until their HPLC signals were totally disappeared at 240 min. The mono-hydroxylated derivatives of BPA (I-a and I-b), as well as diketo compound (II), were previously detected during the electrochemical degradation of BPA using multiwalled carbon nanotube membranes [60]. It is noteworthy mentioning that the formation of di-hydroxylated BPA by hydroxyl radical-based AOPs including TiO_2 AOPs was previously reported in different studies [61–63], however, with the present LC/Q-TOF-ESI-MS experimental method, di-hydroxylated BPA was not detected. The current byproducts 4-isopropenyl phenol (III-a) and 4-hydroxyacetophenone (IV) were also identified by Sunasee et al. during the degradation of BPA by TiO_2 sonophotocatalytic AOP [61]. Despite the number of studies conducted on BPA degradation by AOPs, compounds V and VI were, to the best of our knowledge, newly identified in the current study.
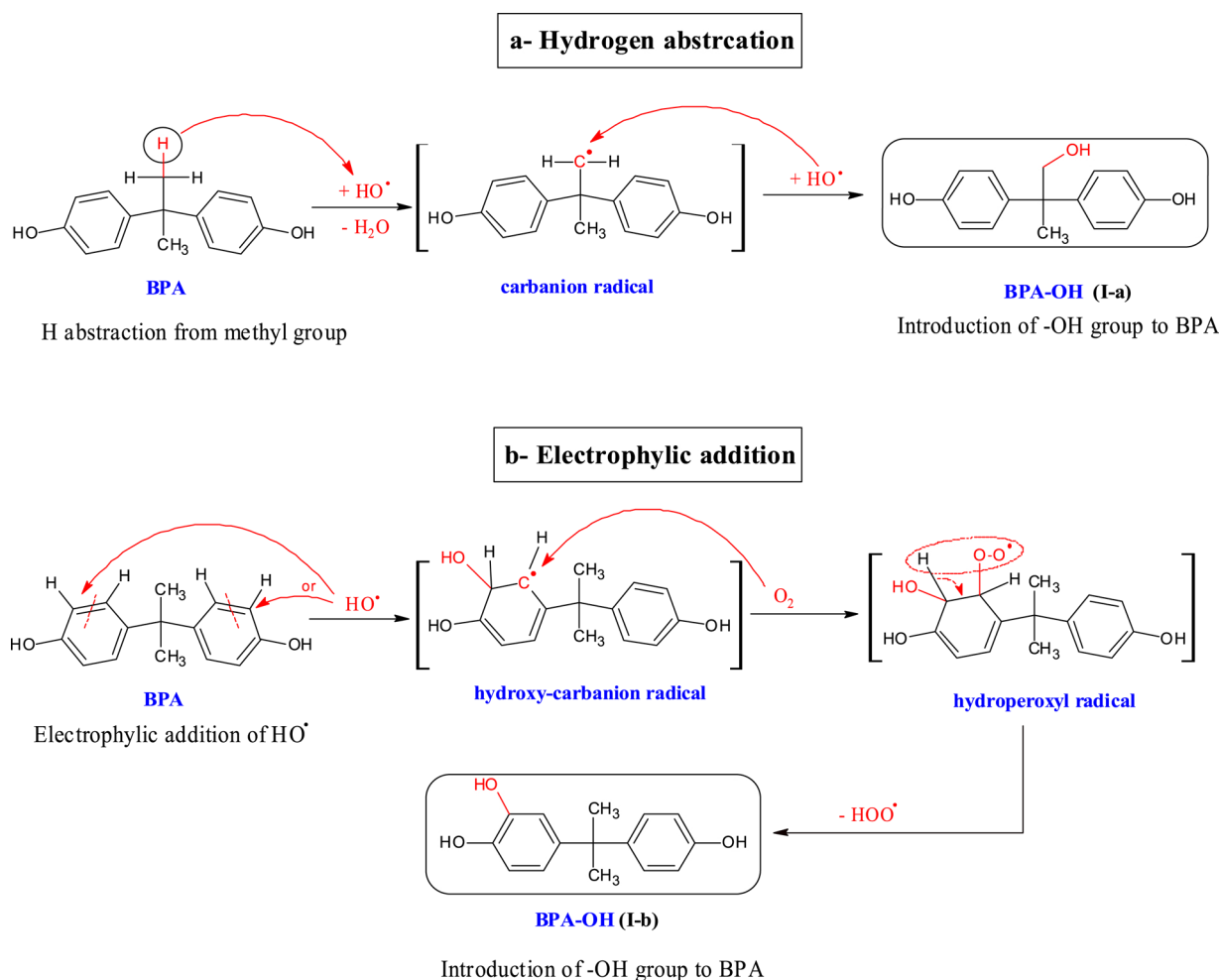
Scheme 2. BPA hydroxylation mechanisms.
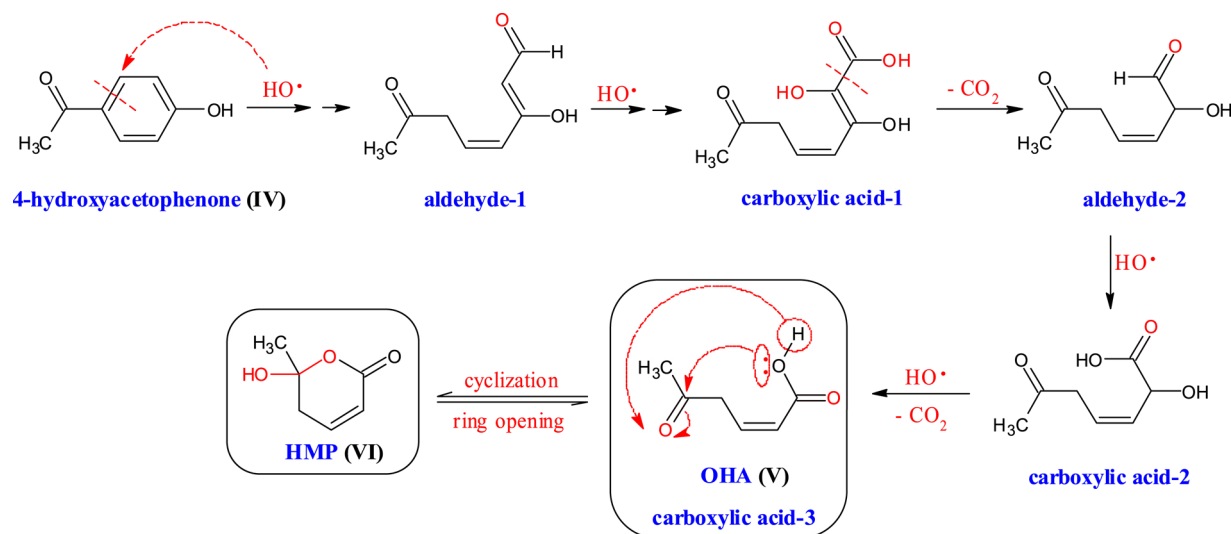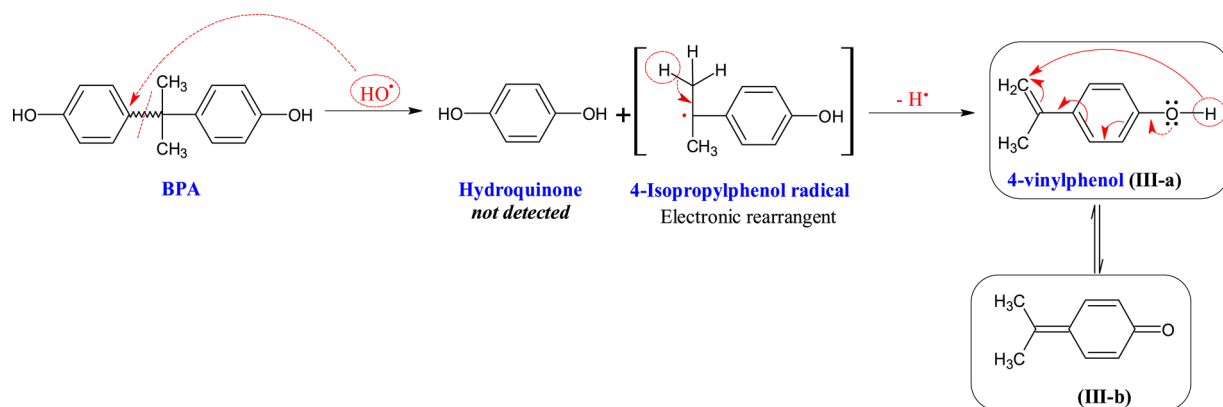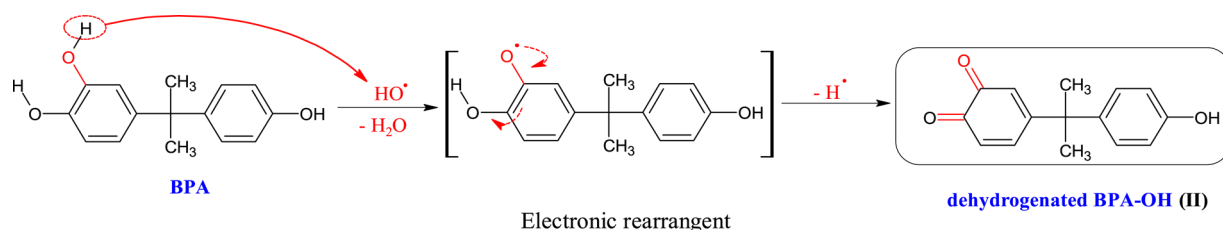
3.3.2. Oxidation pathways

Scheme 1 demonstrates the proposed pathways of BPA photocatalytic degradation by simulated solar light/2.0NBT-350. The main oxidation routes of BPA comprised successive hydroxylation, aromatic ring elimination, ring opening and cyclization of aliphatic compounds.

3.3.2.1. BPA hydroxylation.
Hydroxylation of aromatic compounds by ˙OH-based AOPs is believed to be the primary step of the following sequential ring cleavage and ultimate mineralization of the compound. Thus, several researchers have reported the detection of mono- and poly-hydroxylated derivatives of the parent organic contaminants during AOPs [64]. The formation of hydroxylated aromatic compounds due to ˙OH attack usually occurs via two major mechanisms; a hydrogen abstraction from a carbon atom containing α-hydrogen, and an electrophilic addition to π-systems [65]. Giving that BPA structure encompasses two phenyl rings (i.e., π-systems) as well as α-hydrogen attached to C_{14} and C_{15}, thus, the formation of mono-hydroxylated BPA (BPA−OH) was suggested to take place according to Schemes 2a and b.

In 2003, Watanabe et al. revealed the tendency of two methyl groups (C_{14} and C_{15}) of BPA to adsorb onto TiO_2 catalyst, as a result, they decompose instantly after being attacked by hydroxyl radicals generated at the catalyst surface [66]. Similarly, BPA−OH was primarily produced in the current study via ˙OH attack to C_{14} or C_{15}, with the subsequent abstraction of α-hydrogen to release a water molecule and a BPA radical adduct (i.e., a less stable form of BPA), followed by reaction with another hydroxyl radical to form BPA−OH (I-a; Scheme 2a). Analogous formations of hydroxylated byproducts via H-abstraction mechanism were previously revealed in various hydroxyl radical-based AOPs [67,68]. According to electric charge distribution on BPA, the carbon atoms in *ortho*-position to OH groups in BPA (i.e., C_3, C_5, C_9, and C_{11},) were the most negatively partially charged locations [69]. Moreover, hydroxyl radical cations were suggested to be highly reactive towards these specific carbon atoms to form BPA hydroxylated byproducts [69]. Accordingly, the second mechanism of BPA−OH formation comprised ˙OH addition to C_3, C_5, C_9, or C_{11} of BPA to generate hydroxy-carbanion radical that instantly reacted with the molecular oxygen to form hydroperoxyl radical adduct, followed by HOO˙ release and ultimate formation of BPA−OH (I-b, Scheme 2b). With the successive attacks of ˙OH, a second BPA hydroxylation could also appear via the above two mechanisms to produce di-hydroxylated BPA (m/z 259), though, with the current analysis method we could only detect the monohydroxylated byproducts. Analogous formations of mono- and di-hydroxylated BPA were previously suggested during photocatalytic degradation of BPA by TiO_2 [57,61].

The formation of compound II was hypothesized to take place via two possible routes. The first route was derived by ˙OH and comprised abstraction of a hydrogen atom from OH in the L-ring of compound I-b to generate a water molecule and a radical adduct of BPA−OH, followed by electronic rearrangement and a loss of another hydrogen atom to form the more stable dehydrogenated derivative of BPA−OH (Scheme 3). The second route involved direct oxidation of compound I-b by h^+ on the surface of 2.0NBT-350 [64]. The formation of byproduct II during the photocatalytic degradation of BPA and structurally similar compounds was documented in various recent studies [57,70,71].

Scheme 3. Dehydrogenation mechanism.

Scheme 4. Ring elimination mechanism.

Scheme 5. Ring opening and cyclization.

3.3.2.2. Elimination of aromatic ring. According to the frontier electron density on the carbon atoms of BPA, C_1 and C_7 were illustrated to be highly electron-rich positions with high affinity towards ˙OH attack [66]. Thus, BPA was speculated to be attacked by ˙OH at C_1 or C_7 positions followed by bond rupture and splitting of the BPA phenyl rings into hydroquinone and 4-isopropylphenol radical (*not detected in the current study*). Via a series of electronic rearrangement on the last radical, compounds III-a and/or III-b were produced, Scheme 4. The byproducts I-b and II were also suggested to be successively attacked by ˙OH at C_1 position to eventually generate III-a and III-b via the same mechanism.

The formation of byproduct IV (4-hydroxyacetophenone) could be explained by i) sequential attacks of hydroxyl radicals to BPA and its hydroxylated byproducts I and II with the further elimination of methyl group, and by ii) addition of OH to C_{13} on in III-a and III-b, followed by elimination of $-CH_3$ group and electronic rearrangement. Indeed, the

revealed many pathways of IV formation explained its fast evolution profile during the photocatalytic degradation of BPA (Fig. 8).

3.3.2.3. Ring opening and cyclization. Oxidation of aromatic compounds by AOPs typically involves bond breakdown and ring opening with the generation of several hydroxylated byproducts as well as aldehyde and carboxylic compounds [72,73]. Similar observations were found in the current study via the simultaneous detection of carboxylic acid OHA (V, m/z: 127i) and its cyclic form HMP (VI, m/z: 127ii) at as early as 15 min of the reaction (Scheme 5). These compounds formed via ring opening mechanism followed by sequential oxidation and decarboxylation processes of compounds IV (Scheme 5). The π-bond ($C_7 = C_8$) in compound IV was suggested to rupture and yield a transient aldehyde-1 derivative that was further oxidized to carboxylic acid-1. The latter underwent a series of decarboxylation to yield aldehyde-2 that was instantly oxidized to carboxylic acid-2 after CO_2 release.

Finally, the byproducts V (carboxylic acid-3) and VI could occur via decarboxylation of carboxylic acid-2. The compounds aldehyde-1, aldehyde-2, carboxylic acid-1 and carboxylic acid-2 were not detected in our study, nevertheless, similar degradation mechanisms were reported in earlier studies [72,73].

4. Conclusion

N- and B- co-doped TiO_2 nanoparticles (NBT) were hydrothermally synthesized using borane as a novel substrate for both dopants atoms. All synthesized materials, including pristine TiO_2, existed in anatase phase as determined by XRD and HR-TEM analysis. This result was confirmed via simulation of SAED micrographs using the software CrysTBox v 1.10. The average particle size of 20.6 and 12.9 nm for TiO_2 and NBT, respectively, were calculated from TEM images using ImageJ software (version 1.5i). TiO_2 materials possessed higher BET surface area upon doping, with the highest value of 108.5 m^2/g was recorded for 2.0NBT-350. XPS analysis confirmed the incorporation of N and B atoms into TiO_2 lattice via substitution of O and/or Ti, and interstitial incorporation mechanisms. The optical properties of TiO_2 enhanced significantly after doping. The effective band gaps of photocatalysts were in the following order $TiO_2 \sim 0.8NT$-400 (2.82 eV) > 0.9NT-350 (2.80 eV) > 2.4NBT-350 (2.78 eV) > 2.0NBT-350 (2.72 eV). No apparent degradation in BPA was observed under dark and simulated solar light only conditions. In terms of reaction kinetics, simulated solar light/2.0NBT-350 was the most efficient AOP system for BPA degradation. Catalyst overdoses and high BPA concentrations inhibited the kinetics photocatalytic system. Scavenger experiments revealed $^{\cdot}$OH was the major oxidant in the system, while h^+ and other reactive species (e.g., $HOO^{\cdot}$ and $O_2^{\cdot-}$) were only responsible for minor degradation in BPA. Similar BPA removal efficiencies were obtained over three consecutive catalyst reuses. Removal rate of BPA in SWI water was lower as compared to in clean water, which was rationalized by the greater TOC and alkalinity contents of SWI water. Using LC/Q-TOF-ESI-MS analysis, six byproducts, including two new compounds were identified. The BPA oxidation routes comprised successive BPA hydroxylation, elimination of an aromatic ring, ring opening and cyclization of aliphatic compounds. This study on N- and B- co-doped TiO_2 nanoparticles not only further advances the understanding of doped titania but could also be considered a promising demonstration for controlled design and synthesis of visible-light-active photocatalysts, for environmental applications, especially for the treatment of BPA-contaminated water.

Acknowledgments

Appendix A. Supplementary data

Supplementary material related to this article can be found, in the online version, at doi:https://doi.org/10.1016/j.apcatb.2018.09.039.

References

[1] A. Burke, S. Ito, H. Snaith, U. Bach, J. Kwiatkowski, M. Grätzel, The function of a TiO_2 compact layer in dye-sensitized solar cells incorporating "planar" organic dyes, Nano Lett. 8 (2008) 977–981.
[2] K. Nakata, A. Fujishima, TiO_2 photocatalysis: design and applications, J. Photochem. Photobiol., C 13 (2012) 169–189.
[3] S.-Y. Lee, S.-J. Park, TiO_2 photocatalyst for water treatment applications, J. Ind. Eng. Chem. 19 (2013) 1761–1769.
[4] G.L. Chiarello, M.V. Dozzi, E. Selli, TiO_2-based materials for photocatalytic hydrogen production, J. Energy Chem. 26 (2017) 250–258.
[5] W. Zhou, W. Li, J.-Q. Wang, Y. Qu, Y. Yang, Y. Xie, K. Zhang, L. Wang, H. Fu, D. Zhao, Ordered mesoporous Black TiO_2 as highly efficient hydrogen evolution photocatalyst, J. Am. Chem. Soc. 136 (2014) 9280–9283.
[6] W. Zhou, F. Sun, K. Pan, G. Tian, B. Jiang, Z. Ren, C. Tian, H. Fu, Well-Ordered large-pore mesoporous anatase TiO_2 with remarkably High thermal stability and improved crystallinity: preparation, characterization, and photocatalytic performance, Adv. Funct. Mater. 21 (2011) 1922–1930.
[7] Z. Xing, J. Zhang, J. Cui, J. Yin, T. Zhao, J. Kuang, Z. Xiu, N. Wan, W. Zhou, Recent advances in floating TiO_2-based photocatalysts for environmental application, Appl. Catal. B 225 (2018) 452–467.
[8] F.-t. Li, Y. Zhao, Y.-j. Hao, X.-j. Wang, R.-h. Liu, D.-s. Zhao, D.-m. Chen, N-doped P25 TiO_2–amorphous Al_2O_3 composites: one-step solution combustion preparation and enhanced visible-light photocatalytic activity, J. Hazard. Mater. 239–240 (2012) 118–127.
[9] A. Hu, A. Apblett, Nanotechnology for Water Treatment and Purification, Springer International Publishing, 2014.
[10] E. Grabowska, A. Zaleska, J.W. Sobczak, M. Gazda, J. Hupka, Boron-doped TiO_2: characteristics and photoactivity under visible light, Procedia Chem. 1 (2009) 1553–1559.
[11] S.A. Ansari, M.M. Khan, M.O. Ansari, M.H. Cho, Nitrogen-doped titanium dioxide (N-doped TiO_2) for visible light photocatalysis, New J. Chem. 40 (2016) 3000–3009.
[12] L.G. Devi, R. Kavitha, Enhanced photocatalytic activity of sulfur doped TiO_2 for the decomposition of phenol: a new insight into the bulk and surface modification, Mater. Chem. Phys. 143 (2014) 1300–1308.
[13] M.V. Dozzi, C. D'Andrea, B. Ohtani, G. Valentini, E. Selli, Fluorine-doped TiO_2 materials: photocatalytic activity vs time-resolved photoluminescence, J. Phys. Chem. C 117 (2013) 25586–25595.
[14] G. Wu, T. Nishikawa, B. Ohtani, A. Chen, Synthesis and characterization of carbon-doped TiO_2 nanostructures with enhanced visible light response, Chem. Mater. 19 (2007) 4530–4537.
[15] N.O. Gopal, H.-H. Lo, T.-F. Ke, C.-H. Lee, C.-C. Chou, J.-D. Wu, S.-C. Sheu, S.-C. Ke, Visible light active phosphorus-doped TiO_2 nanoparticles: an EPR evidence for the enhanced charge separation, J. Phys. Chem. C 116 (2012) 16191–16197.
[16] G. Liu, Y. Zhao, C. Sun, F. Li, G.Q. Lu, H.M. Cheng, Synergistic effects of B/N doping on the visible-light photocatalytic activity of mesoporous TiO_2, Angew. Chem. Int. Ed. 47 (2008) 4516–4520.
[17] G. Zhang, Y.C. Zhang, M. Nadagouda, C. Han, K. O'Shea, S.M. El-Sheikh, A.A. Ismail, D.D. Dionysiou, Visible light-sensitized S, N and C co-doped polymorphic TiO_2 for photocatalytic destruction of microcystin-LR, Appl. Catal. B 144 (2014) 614–621.
[18] A. Careghini, A.F. Mastorgio, S. Saponaro, E. Sezenna, Bisphenol A, nonylphenols, benzophenones, and benzotriazoles in soils, groundwater, surface water, sediments, and food: a review, Environ. Sci. Pollut. Res. 22 (2015) 5711–5741.
[19] Y.Q. Huang, C.K.C. Wong, J.S. Zheng, H. Bouwman, R. Barra, B. Wahlström, L. Neretin, M.H. Wong, Bisphenol A (BPA) in China: a review of sources, environmental levels, and potential human health impacts, Environ. Int. 42 (2012) 91–99.
[20] U.S. EPA, A. Bisphenol, Action Plan, U.S. Environmental Protection, Agency, Washington, 2010.
[21] Orange_County_Water_District, Ground Water Replenishment System-Annual Reports, 2017 GWRS Annual Report, Accessed on Aug 28th (2018).
[22] E.W. Rice, L. Bridgewater, A.P.H. Association, A.W.W. Association, W.E. Federation, Standard Methods for the Examination of Water and Wastewater, American Public Health Association, 2012.
[23] F.-t. Li, X.-j. Wang, Y. Zhao, J.-x. Liu, Y.-j. Hao, R.-h. Liu, D.-s. Zhao, Ionic-liquid-assisted synthesis of high-visible-light-activated N–B–F-tri-doped mesoporous TiO_2 via a microwave route, Appl. Catal. B 144 (2014) 442–453.
[24] M. Sahni, B.R. Locke, Quantification of hydroxyl radicals produced in aqueous phase pulsed electrical discharge reactors, Ind. Eng. Chem. Res. 45 (2006) 5819–5825.
[25] G. Zhang, Y.C. Zhang, M. Nadagouda, C. Han, K. O'Shea, S.M. El-Sheikh, A.A. Ismail, D.D. Dionysiou, Visible light-sensitized S, N and C co-doped polymorphic TiO 2 for photocatalytic destruction of microcystin-LR, Appl. Catal. B 144 (2014) 614–621.
[26] F. Peng, L. Cai, L. Huang, H. Yu, H. Wang, Preparation of nitrogen-doped titanium dioxide with visible-light photocatalytic activity using a facile hydrothermal method, J. Phys. Chem. Solids 69 (2008) 1657–1664.
[27] D.C. Chateigner, Xiaolong Ciriotti, Marco Downs, Robert T. Gražulis, Saulius Kaminsky, Werner Le Bail, Armel Lutterotti, Luca Matsushita, Yoshitaka Moeck, Peter Murray-Rust, Peter Olozábal, Miguel Quirós Rajan, Hareesh Yokochi, F.T. Alexandre, Crystallography Open Database, (2017).
[28] M. Klinger, A. Jäger, Crystallographic Tool Box (CrysTBox): automated tools for transmission electron microscopists and crystallographers, J. Appl. Crystallogr. 48 (2015) 2012–2018.

[29] S.Y. Choi, M. Mamak, N. Coombs, N. Chopra, G.A. Ozin, Thermally stable two-dimensional hexagonal mesoporous nanocrystalline anatase, meso-nc-TiO$_2$: bulk and crack-free thin film morphologies, Adv. Funct. Mater. 14 (2004) 335–344.

[30] S.S. Kumar, P. Venkateswarlu, V.R. Rao, G.N. Rao, Synthesis, characterization and optical properties of zinc oxide nanoparticles, Int. Nano Lett. 3 (2013) 30.

[31] C. Dette, M.A. Pérez-Osorio, C.S. Kley, P. Punke, C.E. Patrick, P. Jacobson, F. Giustino, S.J. Jung, K. Kern, TiO2 anatase with a bandgap in the visible region, Nano Lett. 14 (2014) 6533–6538.

[32] N. Masahashi, M. Oku, Superhydrophilicity and XPS study of boron-doped TiO$_2$, Appl. Surf. Sci. 254 (2008) 7056–7060.

[33] T. Lin, C. Yang, Z. Wang, H. Yin, X. Lü, F. Huang, J. Lin, X. Xie, M. Jiang, Effective nonmetal incorporation in black titania with enhanced solar energy utilization, Energy Environ. Sci. 7 (2014) 967–972.

[34] J. Zhu, F. Chen, J. Zhang, H. Chen, M. Anpo, Fe^{3+}-TiO$_2$ photocatalysts prepared by combining sol–gel method with hydrothermal treatment and their characterization, J. Photochem. Photobiol. A 180 (2006) 196–204.

[35] J. Liu, Q. Zhang, J. Yang, H. Ma, M.O. Tade, S. Wang, J. Liu, Facile synthesis of carbon-doped mesoporous anatase TiO$_2$ for the enhanced visible-light driven photocatalysis, Chem. Commun. 50 (2014) 13971–13974.

[36] R. Leary, A. Westwood, Carbonaceous nanomaterials for the enhancement of TiO$_2$ photocatalysis, Carbon 49 (2011) 741–772.

[37] V. Kiran, S. Sampath, Enhanced raman spectroscopy of molecules adsorbed on carbon-doped TiO$_2$ obtained from titanium carbide: a visible-light-assisted renewable substrate, ACS Appl. Mater. Interfaces 4 (2012) 3818–3828.

[38] D. Quiñones, A. Rey, P.M. Álvarez, F. Beltrán, G.L. Puma, Boron doped TiO$_2$ catalysts for photocatalytic ozonation of aqueous mixtures of common pesticides: diuron, o-phenylphenol, MCPA and terbuthylazine, Appl. Catal., B 178 (2015) 74–81.

[39] H.-S. Son, G. Ko, K.-D. Zoh, Kinetics and mechanism of photolysis and TiO$_2$ photocatalysis of triclosan, J. Hazard. Mater. 166 (2009) 954–960.

[40] G. Zeng, C. Zhang, G. Huang, J. Yu, Q. Wang, J. Li, B. Xi, H. Liu, Adsorption behavior of bisphenol a on sediments in xiangjiang River, Central-south China, Chemosphere 65 (2006) 1490–1499.

[41] B. Wang, F. Wu, P. Li, N. Deng, UV-light induced photodegradation of bisphenol a in water: kinetics and influencing factors, React. Kinet. Catal. Lett. 92 (2007) 3–9.

[42] C.-H. Lu, Y. Wang, Y. Li, H.-H. Yang, X. Chen, X.-R. Wang, Bifunctional superparamagnetic surface molecularly imprinted polymer core-shell nanoparticles, J. Mater. Chem. 19 (2009) 1077–1079.

[43] R. Asahi, T. Morikawa, T. Ohwaki, K. Aoki, Y. Taga, Visible-light photocatalysis in nitrogen-doped titanium oxides, science 293 (2001) 269–271.

[44] J. Schneider, M. Matsuoka, M. Takeuchi, J. Zhang, Y. Horiuchi, M. Anpo, D.W. Bahnemann, Understanding TiO$_2$ photocatalysis: mechanisms and materials, Chem. Rev. 114 (2014) 9919–9986.

[45] P. Hegedűs, E. Szabó-Bárdos, O. Horváth, K. Horváth, P. Hajós, TiO$_2$-mediated photocatalytic mineralization of a Non-ionic detergent: comparison and combination with other advanced oxidation procedures, Materials 8 (2015) 231–250.

[46] X. Pang, C. Chen, H. Ji, Y. Che, W. Ma, J. Zhao, Unraveling the photocatalytic mechanisms on TiO$_2$ surfaces using the oxygen-18 isotopic label technique, Molecules 19 (2014) 16291–16311.

[47] W. Zhang, B. Yang, J. Chen, Effects of calcination temperature on preparation of boron-doped TiO$_2$ by sol-gel method, Int. J. Photoenergy 2012 (2012).

[48] J.-M. Herrmann, Heterogeneous photocatalysis: fundamentals and applications to the removal of various types of aqueous pollutants, Catal. Today 53 (1999) 115–129.

[49] F. Shahrezaei, Y. Mansouri, A. Zinatizadeh, A. Akhbari, Photocatalytic degradation of aniline using TiO$_2$ nanoparticles in a vertical circulating photocatalytic reactor, Int. J. Photoenergy 2012 (2012).

[50] J. Saien, S. Khezrianjoo, Degradation of the fungicide carbendazim in aqueous solutions with UV/TiO 2 process: optimization, kinetics and toxicity studies, J. Hazard. Mater. 157 (2008) 269–276.

[51] K.A. Connors, Chemical Kinetics: The Study of Reaction Rates in Solution, VCH, 1990.

[52] X.-j. Wang, W.-y. Yang, F.-t. Li, Y.-b. Xue, R.-h. Liu, Y.-j. Hao, In situ microwave-assisted synthesis of porous N-TiO$_2$/g-C3N4 heterojunctions with enhanced visible-light photocatalytic properties, Ind. Eng. Chem. Res. 52 (2013) 17140–17150.

[53] A. Al-Anazi, W.H. Abdelraheem, C. Han, M.N. Nadagouda, L. Sygellou, M.K. Arfanis, P. Falaras, V.K. Sharma, D.D. Dionysiou, Cobalt ferrite nanoparticles

[54] with controlled composition-peroxymonosulfate mediated degradation of 2-phenylbenzimidazole-5-sulfonic acid, Appl. Catal., B 221 (2018) 266–279.

[54] Y. Son, V. Mishin, W. Welsh, S.-E. Lu, J.D. Laskin, H. Kipen, Q. Meng, A novel High-throughput approach to measure hydroxyl radicals induced by airborne particulate matter, Int. J. Environ. Res. Public Health 12 (2015) 13678–13695.

[55] B. Höbel, C. von Sonntag, OH-radical induced degradation of ethylenediaminetetraacetic acid (EDTA) in aqueous solution: a pulse radiolysis study, J. Chem. Soc. Perkin Trans. 2 (1998) 509–514.

[56] X. He, M. Pelaez, J.A. Westrick, K.E. O'Shea, A. Hiskia, T. Triantis, T. Kaloudis, M.I. Stefan, A.A. de la Cruz, D.D. Dionysiou, efficient removal of microcystin-LR by UV-C/H2O2 in synthetic and natural water samples, Water Res. 46 (2012) 1501–1510.

[57] A.O. Kondrakov, A.N. Ignatev, F.H. Frimmel, S. Bräse, H. Horn, A.I. Revelsky, Formation of genotoxic quinones during bisphenol A degradation by TiO$_2$ photocatalysis and UV photolysis: a comparative study, Appl. Catal. B 160-161 (2014) 106–114.

[58] Y. Nakabayashi, Y. Nosaka, The pH dependence of OH radical formation in photoelectrochemical water oxidation with rutile TiO$_2$ single crystals, PCCP 17 (2015) 30570–30576.

[59] A. Al-Anazi, W.H. Abdelraheem, C. Han, M.N. Nadagouda, L. Sygellou, M.K. Arfanis, P. Falaras, V.K. Sharma, D.D. Dionysiou, Cobalt ferrite nanoparticles with controlled composition-peroxymonosulfate mediated degradation of 2-phenylbenzimidazole-5-sulfonic acid, Appl. Catal. B (2017).

[60] A.R. Bakr, M.S. Rahaman, Removal of bisphenol A by electrochemical carbon-nanotube filter: influential factors and degradation pathway, Chemosphere 185 (2017) 879–887.

[61] S. Sunasee, K.T. Wong, G. Lee, S. Pichiah, S. Ibrahim, C. Park, N.C. Kim, Y. Yoon, M. Jang, Titanium dioxide-based sonophotocatalytic mineralization of bisphenol a and its intermediates, Environ. Sci. Pollut. Res. (2017) 1–12.

[62] R.A. Torres, F. Abdelmalek, E. Combet, C. Pétrier, C. Pulgarin, a comparative study of ultrasonic cavitation and Fenton's reagent for bisphenol A degradation in deionised and natural waters, J. Hazard. Mater. 146 (2007) 546–551.

[63] R.A. Torres-Palma, J.I. Nieto, E. Combet, C. Pétrier, C. Pulgarin, An innovative ultrasound, Fe^{2+} and TiO$_2$ photoassisted process for bisphenol a mineralization, Water Res. 44 (2010) 2245–2252.

[64] C. Guo, M. Ge, L. Liu, G. Gao, Y. Feng, Y. Wang, Directed synthesis of mesoporous TiO$_2$ microspheres: catalysts and their photocatalysis for bisphenol a degradation, Environ. Sci. Technol. 44 (2009) 419–425.

[65] C. Iuga, R. Esquivel Olea, A. Vivier-Bunge, Mechanism and kinetics of the OH· radical reaction with formaldehyde bound to an Si(OH)$_4$ monomer, J. Mex. Chem. Soc. 52 (2008) 36–46.

[66] N. Watanabe, S. Horikoshi, H. Kawabe, Y. Sugie, J. Zhao, H. Hidaka, Photodegradation mechanism for bisphenol a at the TiO$_2$/H$_2$O interfaces, Chemosphere 52 (2003) 851–859.

[67] Y. Guo, Y. Wang, C. Hu, Y. Wang, E. Wang, Y. Zhou, S. Feng, Microporous polyoxometalates POMs/SiO$_2$: synthesis and photocatalytic degradation of aqueous organocholorine pesticides, Chem. Mater. 12 (2000) 3501–3508.

[68] S. Khan, X. He, J.A. Khan, H.M. Khan, D.L. Boccelli, D.D. Dionysiou, Kinetics and mechanism of sulfate radical- and hydroxyl radical-induced degradation of highly chlorinated pesticide lindane in UV/peroxymonosulfate system, Chem. Eng. J. 318 (2017) 135–142.

[69] K. Nomiyama, T. Tanizaki, T. Koga, K. Arizono, R. Shinohara, Oxidative degradation of BPA using TiO$_2$ in water, and transition of estrogenic activity in the degradation pathways, Arch. Environ. Contam. Toxicol. 52 (2007) 8–15.

[70] V. Repousi, A. Petala, Z. Frontistis, M. Antonopoulou, I. Konstantinou, D.I. Kondarides, D. Mantzavinos, Photocatalytic degradation of bisphenol a over Rh/TiO$_2$ suspensions in different water matrices, Catal. Today 284 (2017) 59–66.

[71] F. Lin, B.E. Cojocaru, L.S. Williams, C.A. Cadigan, C. Tian, M.N. Grecu, H.L. Xin, S. Vyas, V.I. Parvulescu, R.M. Richards, Intermediate selectivity in the oxidation of phenols using plasmonic Au/ZnO photocatalysts, Nanoscale 9 (2017) 9359–9364.

[72] W.H.M. Abdelraheem, X. He, Z.R. Komy, N.M. Ismail, D.D. Dionysiou, Revealing the mechanism, pathways and kinetics of UV254nm/H$_2$O$_2$-based degradation of model active sunscreen ingredient PBSA, Chem. Eng. J. 288 (2016) 824–833.

[73] Y. Ji, L. Zhou, Y. Zhang, C. Ferronato, M. Brigante, G. Mailhot, X. Yang, J.-M. Chovelon, Photochemical degradation of sunscreen agent 2-phenylbenzimidazole-5-sulfonic acid in different water matrices, Water Res. 47 (2013) 5865–5875.